Review

An overview of Direct Laser Deposition for additive manufacturing; Part I: Transport phenomena, modeling and diagnostics

Scott M. Thompson [a,b], Linkan Bian [c], Nima Shamsaei [a,b,*], Aref Yadollahi [a]

[a] Department of Mechanical Engineering, Mississippi State University, Mississippi State, MS 39762, USA
[b] Center for Advanced Vehicular Systems (CAVS), Mississippi State University, Mississippi State, MS 39762, USA
[c] Department of Industrial and Systems Engineering, Mississippi State University, Mississippi State, MS 39762, USA

ARTICLE INFO

ABSTRACT

Laser-based additive manufacturing (LBAM) processes can be utilized to generate functional parts (or prototypes) from the ground-up via layer-wise cladding – providing an opportunity to generate complex-shaped, functionally graded or custom-tailored parts that can be utilized for a variety of engineering applications. Directed Energy Deposition (DED), utilizes a concentrated heat source, which may be a laser or electron beam, with in situ delivery of powder- or wire-shaped material for subsequent melting to accomplish layer-by-layer part fabrication or single-to-multi layer cladding/repair. Direct Laser Deposition (DLD), a form of DED, has been investigated heavily in the last several years as it provides the potential to (i) rapidly prototype metallic parts, (ii) produce complex and customized parts, (iii) clad/repair precious metallic components and (iv) manufacture/repair in remote or logistically weak locations. DLD and Powder Bed Fusion-Laser (PBF-L) are two common LBAM processes for additive metal part fabrication and are currently demonstrating their ability to revolutionize the manufacturing industry; breaking barriers imposed via traditional, 'subtractive' metalworking processes.

This article provides an overview of the major advancements, challenges and physical attributes related to DLD, and is one of two Parts focused specifically on DLD. Part I (this article) focuses on describing the thermal/fluidic phenomena during the powder-fed DLD process, while Part II focuses on the mechanical properties and microstructure of parts manufactured via DLD. In this current article, a selection of recent research efforts – including methodology, models and experimental results – will be provided in order to educate the reader of the thermal/fluidic processes that occur during DLD, as well as providing important background information relevant to DLD as a whole. The thermal/fluid phenomena inherent to DLD directly influence the solidification heat transfer which thus impacts the part's microstructure and associated thermo-mechanical properties. A thorough understanding of the thermal/fluid aspects inherent to DLD is vital for optimizing the DLD process and ensuring consistent, high-quality parts.

© 2015 Elsevier B.V. All rights reserved.

Contents

* Corresponding author at: Department of Mechanical Engineering, Mississippi State University, Box 9552, Mississippi State, MS 39762, USA.
E-mail address: shamsaei@me.msstate.edu (N. Shamsaei).

Nomenclature

A	material constant
A_m	melt pool cross-sectional area, m^2
$A(T)$	laser-surface coupling coefficient
c_p	specific heat capacity of the substrate, J/kg K
C_R	cooling rate, K/s
c_s	speed of sound in the melt pool, m/s
D	densification of ferrous metal powders
d_p	powder/particle diameter, m
E	specific energy, J/mm^2
Fr	Froude number
F_r	the vapor recoil force, N
g	local acceleration due to gravity, m/s^2
G	melt pool thermal gradient, K/m
h	heat transfer coefficient, W/m^2 K
h_{LV}	latent heat of vaporization, J/kg
h_x	local heat transfer coefficient, W/m^2
$\bar{h}_{LV}$	latent heat of vaporization per unit atom, J/mol
ith	number of detector element
K_o	modified Bessel function of the second kind and zero order
l	laser/powder working distance, m
$M_{substrate}$	mass of the substrate, kg
$\dot{m}_c$	mass formation speed, kg/s
$\dot{m}_p$	powder feed rate, kg/s
n	material constant
$N(r,l)$	number of coaxially blown particles per unit volume, or powder volume concentration, m^{-3}
N_{max}	maximum volume concentration
N_o	number of nucleation sites
n_{step}	number of deposition layers along a thin wall
P	laser power, W
q''	heat flux, W/m^2
q''_{laser}	laser heat flux, W/m^2
q''_{loss}	local heat loss, W/m^2
r	distance from the beam centerline, m
$R(\lambda)$	detector response
r_b	beam radius, m
r_B	radial distance in which the surface temperature reaches T_{sat}, m
$r_{b,i}$	radius of the laser beam at the melt pool interface, m
r_m	melt pool radius, m
r_p	characteristic powder stream radius, m
S_i	thermal detector signal
T	absolute temperature, K
$T(x)$	local surface temperature, K
T_∞	environment fluid temperature, K

T_o	independently measured temperature, K
T_{sat}	vaporization temperature of the metal at atmospheric pressure, K
$\bar{T}(x^*, z^*)$	temperature field (x, z coordinates), K
t_e	laser/particle interaction (or exposure) time, s
V_{beam}	laser beam travel speed, m/s
V_{iso}	solidification velocity, m/s
v_p	powder velocity, m/s
$\left\|\frac{\Delta x}{\Delta t}\right\|_e$	rate of melt pool topology deformation due to evaporation, m/s
ΔH_m	latent heat of fusion, J/kg
$\Delta P(r)$	radial variation in vapor pressure, Pa
ΔT_{layer}	temperature rise between layers, K
Δt_{step}	idle time, s
$\partial T/\partial t$	cooling rate at a given location near the melt pool, K/s
$\partial \sigma/\partial T$	surface tension-temperature sensitivity (surface tension coefficient), N/m/K
$\nabla T_l(r, t)$	temperature gradient at the liquidus isotherm, K/m
α_m	absorptivity of the melt pool
α	thermal diffusivity of the metal at liquidus temperature, m^2/s
ε_o	permittivity of free space
η_a	energy efficiency
η_{melt}	melting efficiency
η_p	powder efficiency
θ	angle between the solidification front unit normal vector and the laser beam moving direction
θ_{eff}	contact angle along melt pool three-phase interline
κ	densification coefficient
λ_2	dendrite arm spacing (DAS), μm
$\lambda_e(T)$	temperature-dependent, effective wavelength, μm
$\rho_e(T)$	material's temperature-variant electrical resistivity, Ωm
ρ_L	density of the liquid, kg/m^3
σ_{LV}	liquid/vapor surface tension, N/m
σ_{SL}	surface/liquid surface tension, N/m
σ_{SV}	surface/vapor surface tension, N/m
φ	volume fraction of equiaxed grains
ω	angular frequency of the laser irradiation, rad/s
2D	two dimensional
3D	three dimensional

1. Introduction

1.1. Preface

The mechanical behavior, and thus the 'trustworthiness'/durability, of materials fabricated via laser-based additive manufacturing (LBAM) is currently not well understood. Since

the ultimate mechanical behavior of metallic parts is related to its thermal-history-dependent microstructure, additive manufactured (AM) parts will have different, more anisotropic properties than their wrought counterparts. In order to control their microstructure and resultant mechanical properties, it is vital to understand and predict their thermal gradients, localized-solidification phenomena and residual stresses during the layer-wise manufacturing process. If these events can be effectively modeled as a function of relevant process parameters (e.g. laser power, scan rate, etc.), LBAM can ultimately become a 'hands-off' operation governed by in situ diagnostics and feedback control; providing for application-optimized parts with tailored mechanical properties. As a result, many research efforts have focused on determining the effects of process parameters and design patterns on microstructure and mechanical properties of LBAM parts. One such LBAM process is Direct Laser Deposition (DLD) – which consists of blown powder and in situ laser melting.

Due to the high research activity and breadth of the DLD research topic, this article is divided into two Parts. Part I will focus on DLD fundamentals and the inherent thermal/fluidic phenomena during the build, while Part II focuses more on the material science and mechanical characteristics of DLD-fabricated parts, while also discussing monitoring/control methods for the DLD process. This first Part (herein) aims to function as both (i) an introduction to DLD and (ii) an overview of the current state-of-knowledge of DLD as it pertains to transport phenomena. A somewhat elementary discussion of LBAM and DLD will be provided with important historical achievements and general insights/descriptions of the inter-related physical processes during the build. Intertwined with this explanatory content will be highlighted findings from the open literature – indicating the major achievements in DLD thermal/fluid characterization. Note that this overview article focuses on *powder-fed* Direct Laser Deposition (DLD) for the additive manufacture of *metal* parts.

Heat transfer is the driving force for accomplishing DLD – directly or indirectly affecting part quality and structural integrity as dictated by material-coupled, thermally driven solidification and microstructural evolution. The success of DLD lies within effective layer-wise bonding of material which is accomplished by thermal energy transfer. From 'deposition-to-part', there are many impactful thermal and fluidic phenomena at work, including: melt pool initiation (powder melting), melt pool superheating and solidification, melt pool fluid mechanics and wetting behavior, boundary heat transfer (part-to-environment and vice versa) which includes convection and thermal radiation, and 'intra-part' heat transfer which includes conduction (melt pool to substrate) and heat generation/destruction (related to solid state transformations). Since the thermal/fluidic behavior of the melt pool and intra-part heat transfer can provide significant insight into the final part quality, understanding and optimizing the DLD process requires mastery of the thermal/fluidic phenomena occurring during the build.

Based on the importance of heat transfer during DLD, real-time non-destructive evaluation (NDE) via thermal diagnostics/monitoring continues to aid in predicting post-fabrication properties. Control of thermal behavior thus provides a means to ensure product reproducibility and quality. The measurable thermal signature at the melt pool, as well as the temperature distribution along the part, can be correlated with final part properties so that closed-loop control algorithms can tailor a part for optimal functionality. Residual stress within the part can also be controlled by monitoring and controlling the inherent DLD temperatures.

This article will discuss, in order, the (i) laser and powder delivery of DLD, (ii) melt pool thermal/fluidic behavior, (iii) solidification heat transfer, (iv) sensible heat transfer to/from part, (v) thermal monitoring and (vi) the ongoing challenges and future outlook of DLD. Detailed topics include: laser/powder deposition, heat transfer to/from build surface, melt pool formation and dynamics,

solidification, cooling rates, thermal cycling, the heat affected zone (HAZ), effects of bottom substrate, pyrometry/thermography and more. Analytical, numerical and experimental methods employed to better understand DLD, along with select, major published results, will be provided. Methods for monitoring and controlling the DLD process will also be discussed. Sections 1.2–1.4 provide introductory content related to LBAM and details regarding the development of DLD and its fundamental concepts.

1.2. Background

In the past century, the concept of 'additive' manufacturing (AM) has originated and evolved significantly. In contrast to traditional, 'subtractive' manufacturing methods, AM allows for the generation of a part or prototype from the 'ground-up' as opposed to removing material from an initial (larger) volume or relying on pre-fabricated dies (e.g. as within forging, stamping, casting). The American Society for Testing and Materials (ASTM International) define AM as [1]: "*a process of joining materials to make objects from 3D model data, usually layer upon layer, as opposed to subtractive manufacturing methodologies.*" Additive manufacturing has many aliases, including: solid freeform fabrication (SFF), additive fabrication, additive processing, additive layer manufacturing and more [1]; it may also be referred to and associated solely with, incorrectly at times, rapid prototyping and '3D printing'.

Additive manufacturing (AM) has received considerable attention in the past few decades from both the commercial and academic sectors [2], with over 3500 patents related to AM emerging from 1975 to 2011 [2]. The idea of 'printing' a three-dimensional prototype or part on-demand, as opposed to purchasing or sending dimensioned drawings out-of-house for machining, is alluring to both industry and individuals alike. Time has demonstrated that AM is not just restricted to rapid 'printing' of prototypes, but is also a means for generating fully-functional parts for service in a variety of applications. This offers the potential to reduce production time/costs for low-volume/high-value/complex-shaped components and the opportunity to manufacture in atypical, remote environments – such as forward-moving bases (battlefield) and on space stations.

Additive manufacturing can also reduce the overall time-to-market for new components by accelerating the in-house testing of variously designed prototypes prior to market/end-user introduction. For example, AM allows for rapid generation of visual aids for presentation and engineering analysis resulting in less 'trial-and-error' based learning of a part's flaws. Additive manufacturing can also allow for fabricating traditionally assembled parts as integral components – providing an opportunity to reduce overall weight and number of joints/fasteners [3]. To date, there have been many proven applications of AM including unmanned aerial vehicles (UAVs) [4], fuel nozzles [5] houses [6], tooling [7,8], biomedical implants [9], and more.

The fundamental premise of AM is quite simple; it is a means of creating either a part by effectively joining materials (either like or dissimilar), typically in a layer-by-layer fashion via CNC (computer numerical control) displacement, from imported three-dimensional (3D) model data (e.g. computer-drawn parts). Through AM, a machine can "assemble" a 3D part by bonding materials, with each new layer of material being a manifestation of 3D model cross-sectional data. These models are typically in the form of Computer Aided Drawings (CAD) in the STL (Standard Tessellation Language) file format and are numerically 'sliced' into many fictitious layers/cross-sectional areas which dictate the CNC displacement.

To accomplish effective material joining, the successful combination of material, or feedstock, and energy delivery is required – and these combinations differ with process material and various AM machines. As the process material changes, then so can the

material 'preform' that exists prior to AM, which may be powder, wire, sheets, etc. The typical, ASTM-recognized AM methods are: material extrusion, material jetting, sheet lamination, vat photo-polymerization, binder jetting, directed energy deposition (DED) and powder bed fusion (PBF). Typically, each AM method is tailored for building a specific type of material (e.g. plastics, polymers, composites or metals) as the effective material deposition and joining can be unique. A more detailed description of the various AM methods can be found in Refs. [10–12].

The AM process is traditionally 'open-loop'; however, real-time feedback control can be integrated into the AM machine for ensuring better part quality (as discussed in Part II). Feedback control is accomplished by having a non-destructive monitoring system installed that indirectly measures part quality, for example, through use of infrared thermal imaging – to determine localized hot regions known to manifest to, for example, residual stress or part morphing. Such data obtained by monitoring can be used to adjust the AM process parameters in real-time as to rectify the manufacturing process automatically – providing for a 'hands-off' operation. To ensure correct part dimensions/shape and integrity, post-AM procedures are typically performed; such as excess material removal and heat treatment. In PBF, for example, a 'de-powdering' procedure is required to remove excess metallic powders adjoined to the fabricated part, while parts made via vat photopolymerization may require excess curing time outside the machine. For a target volume, a part built via AM is at risk of being over-dense or under-dense due to the presence of contaminants, voids and/or cavities. The actual volume of the part relative to the targeted volume is referred to the part's net shape, and this net shape is often sought to be zero (i.e. near net shape). As it will be discussed in Part II, the net shape and density of the final part can impact its post-manufactured thermo-mechanical properties.

1.3. Additive manufacturing of metals

When it comes to the AM of metallic parts, the DED and PBF processes are the most proven and feasible methods. Both processes involve the deposition of powder metal (or less common preforms such as wire) and their simultaneous or subsequent melting via a focused thermal energy source. Unlike plastic or polymeric-based AM processes, PBF and DED require an electron beam or laser beam (or any thermal energy source) to accomplish layer-to-layer metallurgical bonding – to overcome the relatively high enthalpy of fusion and melting temperature of metals. When a laser is used for either DED or PBF (as the energy delivery type) the processes can be referred to as a form of Laser-Based Additive Manufacturing (LBAM) while DED can be further specified as Direct Laser Deposition (DLD).

Powder Bed Fusion-Laser (PBF-L), also referred to as Selective Laser Melting (SLM), is used to generate metallic prototypes/parts via the incremental height-wise movement of a table consisting of a compact, uniformly distributed layer of metallic powder that is selectively melted by a focused laser beam. As shown in Fig. 1, a uniform 'bed' of powder is first deposited and then specific regions of the bed are melted by the laser beam in order to build a single layer of the part. The melting pattern, or laser scanning pattern, can be continuous lines or near-random pulses. Upon the completion of a single layer, the powder bed is lowered by the height of the deposited layer, a new bed of powder is deposited with a roller, and the process is repeated. This repetitious process results in excess metal powder which can help in supporting the part during the build and can also result in powder remaining in the part if it consists of passages/channels in the design. The use of PBF-L for generating parts with 'overhanging' structures is advantageous, as these sections can be supported by the un-melted powder bed, thus reducing residual stress formation and the potential of part collapse during the build. The PBF-L process typically occurs in an enclosed,
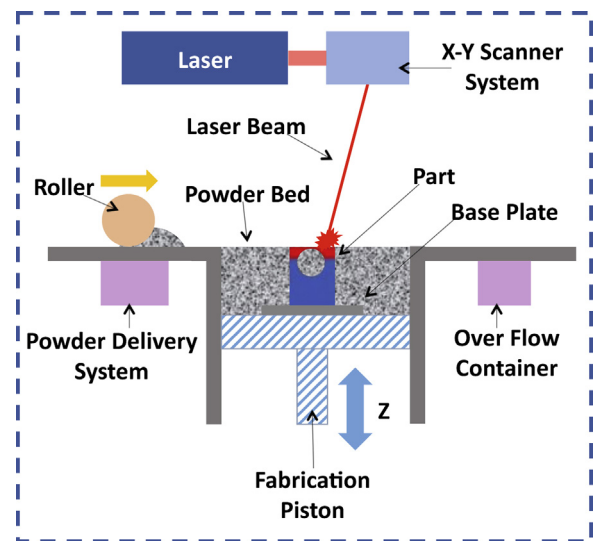

Fig. 1. The Powder Bed Fusion-Laser process.

inert-gas atmosphere as to reduce the oxidization rate of the part during the build. The part is built upon a base plate (i.e. build plate, substrate, platen), and the finished part must be sheared off from the base plate after the AM process. This is typically accomplished by electrical discharge machining (EDM).

Like PBF-L, DLD is a means to build metallic prototypes/parts. However, instead of a separate material and selective energy delivery process, DLD combines the material/energy delivery for simultaneous deposition and part forming within a similar region as shown in Fig. 2. The metal preform can be wire or powder with the latter being significantly more abundant and supported by contemporary DLD machines. Wire-fed DLD provides for better control on the deposition efficiency, while powder preform is typically blown through nozzles and can result in non-used powder accumulation in the DLD machine. Earlier DLD systems consisted of single, coaxial nozzles (coaxial with laser beam) in atmosphere, while current DLD machines may have up to four (or more) nozzles and utilize inert gas as to minimize high oxidization rates inherent for elevated temperature metal processing [13].

The main differences between PBF-L and DLD can be exploited for various applications and end-user needs. PBF-L can provide for finished parts with finer surface quality, but a de-powdering procedure is required. DLD may require a post-AM machining procedure,
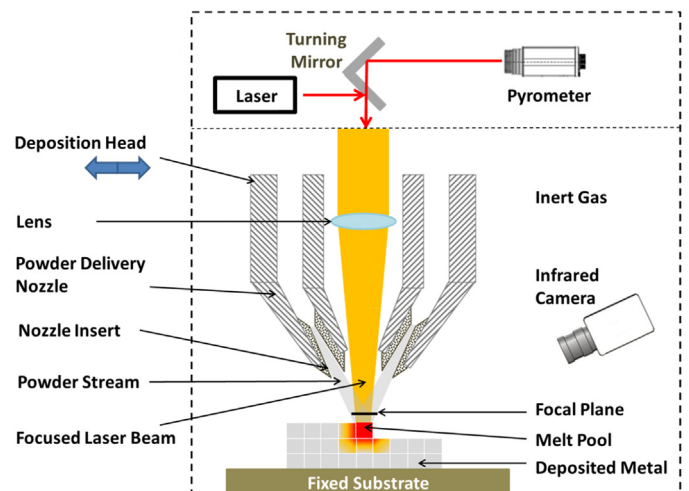

Fig. 2. Blown powder Direct Laser Deposition (DLD) with thermal monitoring.

but the surface quality may not be as fine as a PBF-L part. PBF-L may be more advantageous for construction of 3D structures with overhanging parts – since the powder bed acts as a supporting structure. The lasers utilized for PBF-L typically have lower power (due to finer powder size) than those required for effective DLD. Since DLD does not rely on a pre-deposited layer of metallic powder, it may be used as a means to repair or coat parts via cladding [14–16]. In addition, due to the combined material/energy delivery method, DLD can be readily utilized for creating functional graded/composed parts with varying material/alloy concentrations. Finally, preform mixing can be accomplished with DLD – such as coaxial powder delivery and lateral wire feeding [17,18].

Laser-based additive manufacturing has been a work in progress for many decades – with roots in powder metallurgy, laser welding, arc welding and more. For example, back in the 1930s, the additive manufacture of metals was conceived by using a manual layer-by-layer build-up procedure via arc-welding and high pressure [19]. Harter, circa 1942, explained a process in which molten beads of weld material can be successively deposited to fuse and form a structure built via layer-by-layer fashion [20]. During the 1960s and 1970s, advancements in 'welding-based AM' continued with more patents describing rotary-based, continual arc-welding for the additive manufacture of solid structures and more [21–23].

The paradigm shift in additive metalworking, and the true initiation of LBAM, began circa 1980 with the patents of Housholder and Brown et al. [24,25]. Brown et al. described a process foundational to DLD, while the technology blossomed with patent descriptions by Lewis et al. and Jeantette et al. [26,27]. Housholder provided a technical description similar to PBF-L, however, the modern technical framework and rapid commercialization of PBF-L began with Deckard and Meiners et al. circa 1990 [28–30].

1.4. Direct Laser Deposition

Direct Laser Deposition (DLD), a method for LBAM and type of DED process, utilizes metal wire and/or powder preforms that are directly deposited to a work site accompanied with simultaneous irradiation of a laser beam. Coupled with a moving substrate, DLD provides for a pool of molten metal that travels in space/time – effectively creating a three-dimensional part from zero medium. As shown in Fig. 2, in-line with the deposition head, which can consist of either a single powder-spray nozzle or multiple nozzles, is a focused laser beam. As particles (or wire feedstock) are deposited, the laser beam provides sufficient thermal energy to melt the particles along the deposition path. This creates a molten pool (liquid metal) that, below it, is a heat affected zone (HAZ) with varying penetration depth. Once the deposition of a single layer is complete, the build plate moves via CNC relative to the deposition head and the process is repeated. Thermal monitoring may be implemented through the use of infrared cameras and/or pyrometers [13,31–38]. Such monitoring can be used for DLD feedback control or for data collection. Typical DLD processes require the use of a build plate that is fixed and similar in material composition to that of the material preform. The substrate is the 'stage' in which the additive manufacturing process occurs. Like PBF-L, the finished part(s) must be sheared off from the substrate after the AM process. DLD can be utilized for additive manufacture of a variety of metals and even ceramics – including: Inconel 625, stainless steels, H13 tool steel, titanium alloy, chromium, tungsten and more [35,39–45]. Direct Laser Deposition has also been utilized to successfully manufacture cermet composed of tungsten carbide-cobalt [46].

The DLD process consists of various operating/process parameters. These operating parameters are set, monitored and/or controlled to ensure part quality and build success. The prominent, controllable operating parameters include: laser/substrate relative velocity (traverse speed), laser scanning pattern, laser power, laser beam diameter, hatch spacing, particle/powder feed rate and inter-layer idle time. Such operating parameters are material-dependent and vary with DLD machines (e.g. number of nozzles, nozzle design) and operating environment. Process parameters can be altered for a given material to control structural quality, functional-grading or (intentional) porosity.

The laser-to-substrate traverse speed effectively dictates the length of time DLD takes for a given part geometry and is typically on-the-order of 1–20 mm/s. The laser scanning pattern is set by the operator prior to DLD and dictates the laser position and height-wise positioning of the substrate via CNC. The laser power is the total emitted power from the DLD laser source. This power is typically on-the-order of 100–5000 W while the beam diameter is on-the-order of 1 mm. Laser irradiation is pivotal for joining subsequent layers by melting delivered metallic powders, forming a dynamic molten pool of metal atop solid layers.

Powders can vary in size and shape and in terms of how they are produced. For most DLD applications, the powders are larger in size compared to those used in PBF-L processes. For DLD, it is common to see powders range between 10 and 100 μm and are typically spherical in shape. Spherical-shaped particles can reduce any entrapment of inert gas within the melt pool and can thus lead to a final part with less porosity. Powders for alloyed materials will consist of all alloyed constituents as they are produced from the alloyed metal in its molten state. Gas atomization, water atomization and plasma rotating electrode processes (PREP) are typical means for producing powders effective for DLD application [47]. The particle feed rate is the average mass of particles leaving the DLD nozzle with respect to time and can range between 1–10 g/min (grams per minute). The inter-layer idle time is the finite time elapsed between successive material/energy deposits or layers and can range, for example, from 0 to 1000 s [48–51].

Early concepts of combined energy/material delivery for additive manufacture of metals, including modern DLD, are rooted with the 'welding AM' era – as evidenced by the patents of Kratky and Harter [19,20]. Driven by private industry, early concepts of DLD emerged in circa 1980 as evidenced by a patent from Brown et al. that describes layer-wise, additive deposition via combined laser-powder (or wire) metallurgy [25]. DLD-based technology received only moderate attention through the 1980s. Mehta et al. [52] patented a means to repair metallic articles via the combined utilization of a laser and blown powder in which special attention was given to providing a consistent, continuous flow of powder for the subsequent melting. German-based DLD technology referred to as 'controlled metal build up' emerged in the early 1990s [53,54]. Advancements in combined laser/powder delivery mechanisms (e.g. deposition heads) were also provided by, most notably, Hammeke [55] and Buongiorno [56]. Advancements in SLM occurred, as well – with patents introduced by Deckard and Whitlow et al. [30,57].

Directed Light Fabrication (DLF) was brought forward as a form of single-nozzle, powder-based DLD by Lewis et al. circa 1995 [26,58] and was a technology developed at Los Alamos National Laboratory [59–61]. The DLF technology was demonstrated as a means of combining CAD, CNC and DLD for rapid freeform fabrication of complex shapes – including the building of stainless steel and rhenium parts and utilization of 5 build axes [62,63]. For AISI 316 stainless steel, DLF fabrication provided for a characteristic cooling rate of 10,000 K/s that provided for well-refined microstructures, however Scanning Electron Microscope (SEM) images of the parts indicated substantial presence of non-melted particles within the surface [63].

In the mid-to-late 1990s, researchers at Sandia National Laboratories innovated a process, later trademarked as Laser Engineered Net Shaping (LENS®), which was another a form of powder-based DLD and included multiple nozzles for more effective powder

Laser
- type, power, frequency
- beam profile, diameter and offset
- substrate/laser relative speed
- scanning pattern, idle time
- laser-induced plasma & pressure

Blown Powder Dynamics
- nozzle specifications
- particle feed rate, frequency, efficiency, idle time
- particle/carrier-gas interaction (drag)
- particle/particle interaction (collisions)
- particle/melt pool interaction (mass reflection/absorption)
- body force interaction

Blown Powder Energy Transfer
- laser/powder interaction
  - attenuation, scattering, absorption
- mid-flight pre-heating, melting and evaporation

Melting (Useful Energy Utilization)
- melt pool initiation (melting of submerged powder)
- melt pool/laser interaction (absorption)

Melt Pool Heat Loss
- convection to shielding/carrier gas
- radiation/reflection to surroundings
  - variant emissivity, reflectivity
- melt pool evaporation

Melt Pool Dynamics
- melt pool/powder interaction (splashing, mass addition)
- temperature distribution (superheat)
- radiation transmission
- wetting behavior with pre-deposited layers and gas (surface tension, contact angle variation, oxidization)
- profile stability (boiling, vapor re-coil)
- fluid dynamics (Marangoni convection, density-driven flows, body forces)

Conduction
- Heat Affected Zone (HAZ) volume/depth
- high heat flux transport
- sensible heating/thermal cycling
- substrate interaction (heat sinking effects)

Part Heat Loss
- convection to inert gas
- radiation to surroundings
  - emission, absorption

Solidification
- enthalpy of fusion (melt pool dissolution)
- re-melting of previous layers
- porosity/inert gas entrapment
- heterogeneous nucleation of solid participate
- mushy zone thermo/fluidics

Microstructural Evolution
- dendritic solidification/growth
- dilution of chemical constituents
- mass transfer

Resultant Mechanical Properties
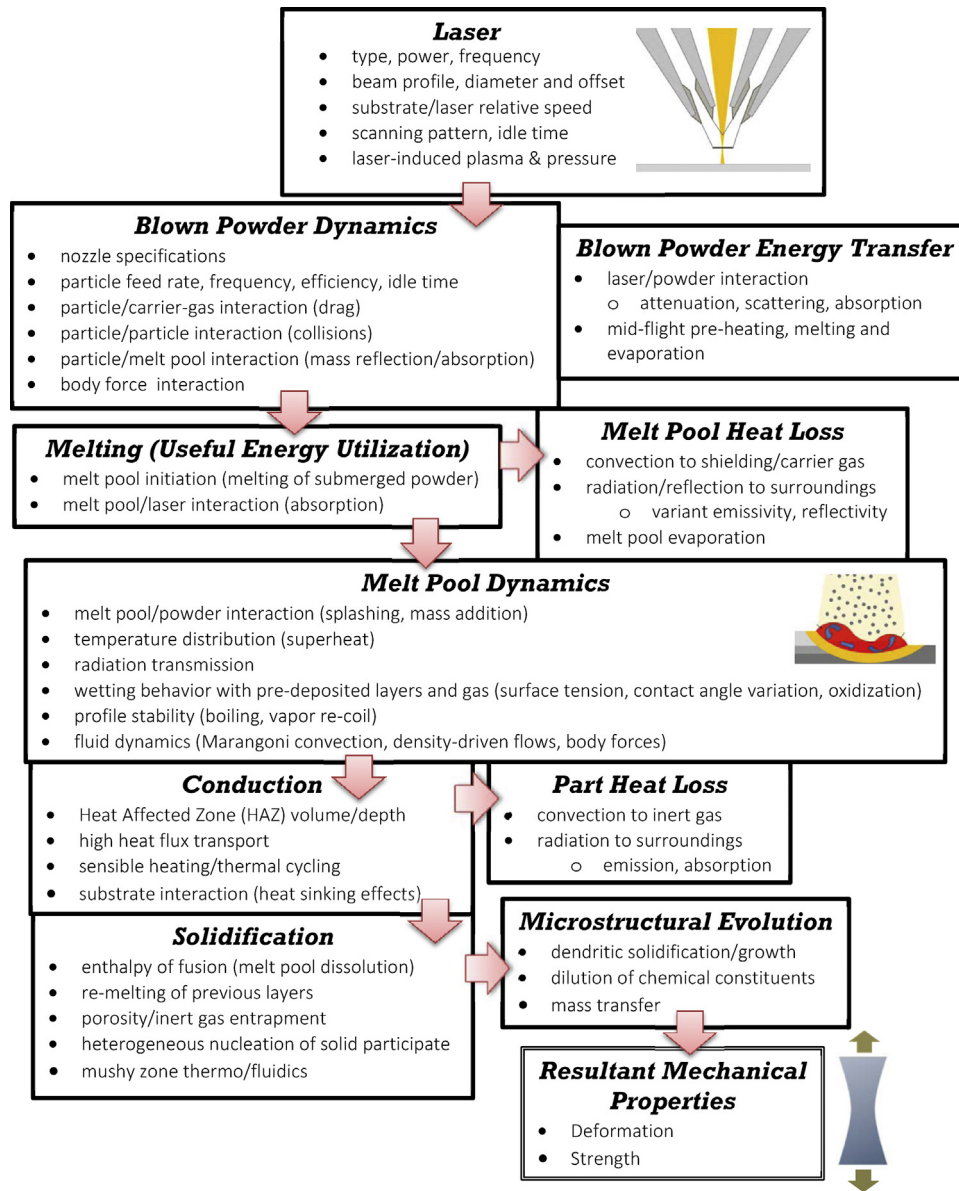- Deformation
- Strength

Fig. 3. Physical events occurring during DLD for given instant in time.

delivery [27,40,64–66]. The LENS process is now the most common means to accomplish powder-based DLD within research and industry. Since LENS is one of the first and, currently, the most successful commercial forms of DLD, LENS has arguably become a proprietary eponym for DLD.

Various other DLD technologies have emerged in the past twenty years – all with varying degrees of success with regard to commercialization and market/research adoption [67–69]. Extending from a literature survey of Costa and Vilar [68], some of these DLD technologies to arise over the years include: laser cladding [70], laser direct casting [71], direct metal deposition (DMD) [72], laser forming or 'Lasform' processing [73], freeform laser consolidation [74,75], laser-aided direct metal/material deposition [76–78], laser-based multi-directional metal deposition [79,80], laser-aided direct rapid manufacturing (LADRM) [81], laser-aided manufacturing process [82–84], laser rapid forming [85], fused deposition of metals [86], laser metal forming [87,88], laser metal deposition shaping [89] and laser-augmented manufacturing (LAM) [90].

Powder-based DLD consists of many interconnected, coupled physical events – all occurring at a very short time scale. For a given instant in time, there are several possible paths for momentum and energy transfer. As shown in Fig. 3, this energy and/or momentum transfer can be categorized as to occur either subsequently or in-parallel. Some of these physical events, in order of approximate occurrence, include: laser delivery, particle/powder delivery (energy and dynamics), laser/powder/gas interactions, melt pool initiation (melting), melt pool energy/stability/morphology, heat loss to environment via thermal radiation and convection, solidification, intra-part conduction, thermal cycling and part-to-substrate conduction. Some of the detailed physical 'sub-events' for each category are provided in Fig. 3. These sub-events within the DLD process have been investigated for the past few decades – either directly in the field of DLD or in similar manufacturing processes, e.g. laser welding/cladding. Each following section in this Overview will highlight major findings relevant to these sub-events.

Affiliated with these physical events are the DLD process parameters and for a given combination of these parameters, for a specific material and machine, a fully dense, structurally sound part can be generated. The sensitivity of the final part quality – as quantified by

its microstructure distribution, micro-hardness, tensile strength, etc. – with regard to the process parameters has been aggressively researched.

The DLD process is rather complex to model/control due to its large process variable space. In fact, Kahlen and Kar [81] demonstrated that the DLD process consists of 19 significant dimensionless parameters. These parameters include, naming only a few: material density, material thermal conductivity, laser beam diameter, laser power, traverse speed, powder feed rate, powder size, gravity and more. Non-dimensional groups/numbers include: process efficiencies – such as energy loss, melting, superheating and powder delivery – and classical non-dimensional numbers such as the: Bond, Froude, Galileo, Prandtl and Reynolds numbers. Geometric non-dimensional parameters were also found and included: non-dimensional length of melt pool, melt pool shape factor and a powder dissolution factor [81]. One advantage of using non-dimensional groups for analyzing a DLD problem is that it removes any material/machine/unit-system dependence.

Although wire-based DLD machines [17,18,91,92] can be beneficial for obtaining increased process efficiency and surface quality, their prominence-in-the-field is significantly less than that of powder-fed DLD. This can be attributed to the fact that blown powder dynamics are easier to control in real-time (less of a response lag) and can be 'tuned' for more precise fabrication of complex geometries. Furthermore, non-used powders can be recycled for later use. Wire-fed DLD is susceptible to vibration and disturbances and require a moderate-to-high degree of control [92] for material deposition which is in contrast to that of powder-fed DLD.

Note that DLD is a specific type of DED in which the energy source is a laser. The DED energy source can also be an electron beam (EB). For DED-EB, a vacuum environment is required, however the energy density and efficiency can be significantly higher than that of DLD [93]. DED-EB is a more attractive means to accomplish DED for either building or repairing parts that are highly reactive to oxygen and has been demonstrated as a means to make functional parts [94,95]. Plasma arcs can also be used as an energy source, such as in plasma deposition manufacturing (PDM) [96].

2. Laser and powder delivery

Powder-based DLD is unique for it allows both material and energy delivery to occur simultaneously at a given location. This is accomplished by the careful combination and integration of blown powder and a relatively high laser power source. Either a single-nozzle or multi-nozzle DLD machine can be used to introduce the continually fed powder stream. For most DLD machines, continuous wave mode lasers are utilized – and focused/de-focused to provide for a sufficient spot diameter for the material processing. The type of laser, and its maximum power capability, varies between various DLD machines.

The laser beam is carried into the DLD chamber and then directed to the deposition region using, for example, a plano-convex lens. For most DLD systems, a Nd:YAG (neodymium-doped yttrium aluminum garnet) laser is utilized [97–99], with typical power ranging between 1 and 5 kW. However, any laser with sufficient power to melt material is acceptable, including CO_2-type [33,41,100] and pulsed-wave lasers [27]. The Nd:YAG laser has been used with success for many laser welding and/or cutting processes in the past due to its incident, spectral radiation being less reflective for most metals (e.g. at a wavelength of 1.067 μm). CO_2-type lasers have wavelengths an order-of-magnitude higher at 10.6 μm and can result in a less energy efficient DLD process. Utilization of CO_2 lasers for DLD can require very high powers, with maximum laser capacities near 18 kW [90]. For most applications, the diameter of the beam is typically on-the-order of millimeters, while the spectral
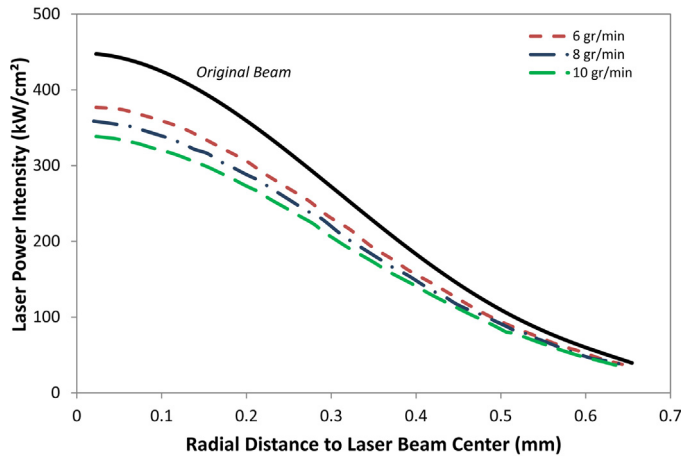

Fig. 4. Laser power intensity vs. radial distance for various powder feed rates (H13 tool steel, laser power = 2200 W, beam diameter = 1.2 mm and traverse speed = 5 mm/s [101].

intensity is near-Gaussian in wave form. Very extreme heat fluxes are experienced within the melt pool. For example, a DLD process operating with a laser at 500 W total power and a beam size of 1 mm provides for an average heat flux in excess of 50,000 W/cm^2.

Laser attenuation occurs due to the blown powder absorbing and scattering the electromagnetic radiation. The radial laser power intensity profile, e.g. in Fig. 4, and ratio of attenuated-to-original laser power, e.g. in Fig. 5, both are affected by the intersecting powder stream feed rate and profile [101]. For fixed laser power, increasing the powder feed rate will result in a slight decrease in the mean temperature of the powder stream and a higher degree of laser attenuation as shown in Fig. 5 for a Gaussian irradiation profile. It may be seen that laser attenuation can be significant and can result in only 75% of original power reaching the melt pool surface [101]. Toward the center of the laser beam (with Gaussian profile), the ratio of attenuated-to-original laser power is lowest – indicating that the powder closest to the beam center absorbs more energy and can even melt mid-flight. To manage laser attenuation, a coherent beam with absorbent wavelengths for the encountered processing temperatures is optimal.

Laser irradiation will depend on the spectral, directional absorptivity of the melt pool and in-flight particles. These particle/melt pool absorptivities are highly transient and depend primarily on surface oxygen content and surface temperatures.
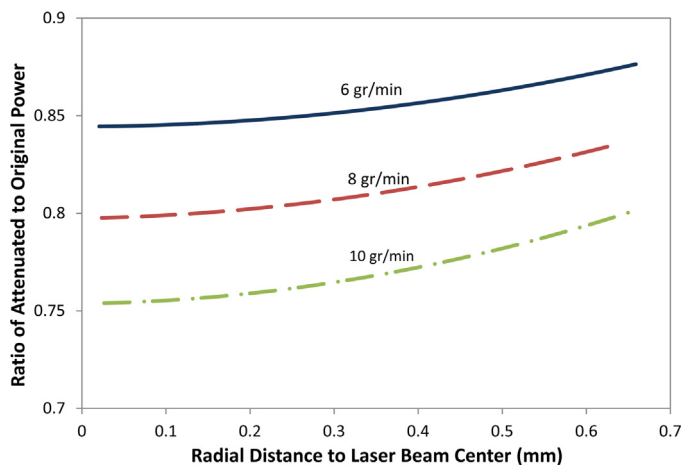

Fig. 5. Ratio of attenuated-to-original power vs. radial distance for various powder feed rates (H13 tool steel, laser power = 2200 W, beam diameter = 1.2 mm and traverse speed = 5 mm/s [101].

Secondary phenomena such as solute partitioning, evaporation and Marangoni convection can affect the variance in absorption/attenuation, as well [102]. To avoid a very challenging radiation problem, many idealize the complex laser attenuation and particle/melt pool absorption via a laser-surface coupling coefficient, or a characteristic absorptivity (absorption coefficient), to scale the input laser power and approximate the incident/delivered power to melt pool region during modeling. This coupling coefficient, which can range between 0.15 and 0.50, will depend on the type of laser utilized (e.g. wavelength) while also depending on surface preparation and temperature [103]. The coupling coefficient can be estimated by utilizing the temperature-dependent electrical resistivity of the material through Bramson's equation or the Hagens-Rubens relationship. For example, the temperature-dependent Hagen-Rubens relationship is stated as, e.g.:

$$A(T) = \sqrt{8\varepsilon_o \omega \rho_e(T)} \tag{1}$$

where $A(T)$ is a laser-surface coupling coefficient, ε_o is the permittivity of free space, ω is the angular frequency of the laser irradiation (rad/s) and $\rho_e(T)$ is the material's temperature-variant electrical resistivity [104,105]. Such expressions can be used to find a time/space/temperature-averaged coefficient for modeling attenuation/absorption effects; specific values (for Nd:YAG) can be 0.28 for AISI 316 SS [51] or 0.36 for Inconel 718 [105]. Experimental methods can also be utilized for characterizing attenuation. For example, the laser energy transfer 'efficiency' for LENS of H13 tool steel was shown to range between 0.30 and 0.50 through the use of a Seebeck envelope calorimeter [106]. For DLD of Ti-6Al-4V, the energy efficiency was found to be around 0.3 with attenuation increasing steadily with higher powder feed rates [107]. Hence, typically less than half of the original laser power is utilized for part formation. An obvious advantage of using electron-sourced beams for DED is that they are less prone to attenuation and the energy transfer efficiency is higher.

For high power scenarios, laser-induced plasma can be formed during DLD and this can significantly affect the absorption of the laser irradiance [108] while also degrading powder efficiency [109]. The primary source for plasma is through the vaporization and ionization of mid-flight particles and can be avoided through the correct combination of powder feed rate and laser power – as to ensure that particles do not overheat prior to melt pool entry [109,110]. Plasma effects can be further minimized through the use of specific shielding gases, such as helium, for example [81]. Laser-induced plasma can become a source for non-linear pressure effects; especially at higher power levels [111]. This positive pressure can help in regulating the amount of vapor escaping the melt pool and also increases with power level [112].

The specific energy (J/mm^2) is a useful means of quantifying energy delivery for unit area of material and is a function of laser power, traverse speed and beam radius, e.g.:

$$E = \frac{P}{2r_b V_{beam}} \tag{2}$$

Utilization of this parameter can decrease the spatial order of process parameters and has been used in similar manufacturing methods such as welding for years. It is a parameter that can be used to predict layer height/width [113] and whether melting can occur for a given set of parameters. Another helpful parameter is the volumetric exposure (J/mm^3) – which can be found by utilizing the beam area instead of its diameter in Eq. (2). Griffith et al. [66] demonstrated that the DLD of Inconel 625 provides for a linear relationship between the layer build-up height and total volumetric exposure.

Laser/particle interaction (or exposure) time can be estimated by taking the quotient of the beam diameter and traverse velocity, e.g.: $t_e = 2r_b/v$, and typically ranges between 0.2 and 8 ms [114].

During beam exposure, the blown particles will undergo sensible heating – increasing in temperature rapidly – depending on their location in the material jet stream and laser beam. In some cases, the particles can evaporate due to excessive power transfer during exposure. Wen and Shin numerically modeled the DLD process, including the effects of particle/laser interaction and demonstrated that particles heat up rapidly when passing through the laser – heating, for example, from 373 K to 1800 K in a matter of seconds, with some particles melting mid-flight [115] while other experiments confirm no melting [66]. There is also evidence that laser processing can lead to powder evaporation after melting – which, in a sense, can be a form of powder sublimation [116]. The main cooling mechanism for mid-flight particles is forced convection with the carrier/shielding gas. The presence of this gas will additionally impact the particle momentum by introducing drag force on the material jet stream and can therefore result in particle deceleration and instability during flight.

When modeling DLD, many estimate the particle temperature to be near its liquidus temperature prior to melt pool entry. Upon entry, particles can melt near instantaneously – within 10^{-4} seconds upon entering a melt pool at uniform melting temperature [109]. Manvatkar et al. [51] utilized a cylindrical heating function to model the sensible heating of particles mid-flight – assuming that the particles were heated, also, in the defocused region of the laser beam. Another method for predicting the laser/particle irradiative heating is via Beer-Lambert attenuation [109]. Superheating of the blown powder will also depend on the size distribution of the powder. Since smaller particles possess a lower thermal capacitance, they can heat up much quicker. For instance, for coaxial DLD of Ti-6Al-4V, 25 μm diameter particles can achieve a maximum temperature on-the-order of 1350 K while 45 μm diameter particles only heat up to approximately 900 K [107].

The powder delivery for a DLD process can be quantified via powder efficiency which is the ratio of powder utilized for final part formation over the actual amount of powder delivered/blown by the system over a given time interval. This powder (or deposition) efficiency depends on the nozzle geometry, angle, as well as the size distribution of the particles utilized. Low deposition efficiency can lead to significant amounts of recycled and/or 'scrapped' metallic powders. These factors can increase the manufacturing costs and complexity by introducing routine cleaning/recycling procedures within the DLD machine. In many cases, the deposition efficiency is quite low. For instance, for LENS of H13 steel – the deposition efficiency was documented as only 0.14 [106].

Metal powder is delivered to the DLD melt pool by an integrated powder delivery system (PDS). The PDS consists primarily of a single coaxial nozzle or multiple nozzles and pumped powder/gas feeding lines. Powder metal originates from a gas-pressurized container that is connected with the powder/gas feed lines and is mixed with a carrier gas. The carrier gas can be substituted or mixed with propellant and such combinations can have an impact on the structural/chemical reactions in the deposited powders and the resultant net shape of the final part [27]. The powder stream delivered to the work site can fluctuate with respect to time at low frequency, but this is detected and rectified by on-board PDS and powder flow sensors. The nozzles are specially designed and positioned as to ensure that the material stream (or powder jet) and laser beam intersect at the laser focal point as shown in Fig. 2. The solid angle and spatiotemporal uniformity of the powder jet can be optimized through careful engineering of the nozzle inserts. The powder stream shape, blown powder speed, laser intensity distribution, and blown powder temperature distribution are all significantly affected by the feeding angle imposed by the nozzle(s) and the imposed powder feeding rate [117]. However, the deposition uniformity is near-independent of the relative laser/substrate (traverse) speed [27]. The number of coaxially blown particles

per unit volume, or powder volume concentration (m^{-3}), can be modeled using an equation in Gaussian form [107]:

$$N(r, l) = N_{\max}(l) \exp\left[-\frac{2r^2}{r_p^2} \right] \qquad (3)$$

where r is the distance from the beam centerline, r_p is the characteristic powder stream radius, l is the laser/powder working distance and $N_{\max}$ is the maximum volume concentration.

The introduction of LENS for DLD brought with it the concept of multi-nozzle deposition. Many 'traditional' DLD methods utilize only one nozzle for powder delivery in which the nozzle is aligned coaxially with the laser. Angled (45°) single-nozzle injection has been investigated, as well [112]. Relative to multi-nozzle DLD systems, such as LENS, it is more difficult to ensure flow uniformity or to direct the material to only specific regions of interest – which is desired for functionally grading. For complex-shaped parts, more directed, multi-nozzle deposition methods can provide for much higher powder/deposition efficiencies [27]. The particle stream diameter should match that of the laser beam in order to increase powder efficiency [27]. Multiple nozzles allow for more precision and this is desirable for parts with added complexity. The deposition process can be monitored to ensure optimal delivery of particles for quality control. [190] used laser Doppler velocimetry for measuring powder flow rates and relative powder density entering the laser beam. In order to increase surface quality, and thus promote powder adhesion, powder injection should occur away from the trailing edge of the melt pool [85]. The degree-of-overlap between the laser beam and the blown powder stream (or powder injection point) will impact part quality, and more specifically the deposition thickness, as well [85].

Liu and Li demonstrated the effect of powder concentration on the build of a thin wall during coaxial-nozzle DLD using a simplified analytical approach [118]. It was found that the laser attenuation and deposition/clad height increases as the powder volume concentration increases or laser beam diameter decreases. They demonstrated that when the centerline of the powder stream is not aligned with that of the laser beam that an irregular deposition/clad profile will occur [118]. Liu and Li also defined a stream-dependent powder efficiency for initiating and sustaining a disk-shaped melt pool. This powder efficiency, η_p, can be calculated as the surface integral of the powder concentration number over the melt pool per total number of particles blown from the nozzle, which simplifies to:

$$\eta_p = 1 - \exp\left(-\frac{2r_m^2}{r_p^2} \right) \qquad (4)$$

where r_m is the melt pool radius. A powder stream with a characteristic radius of $r_p = 1/e^2$ corresponds to the maximum powder number concentration [119]. Based on such a powder efficiency, a mass formation speed, $\dot{m}_c$, can be calculated as: $\dot{m}_c = \eta_p \dot{m}_p$, where $\dot{m}_p$ is the powder feed rate. The mass formation speed decreases with higher traverse speeds and increases for higher laser powers. For sufficient laser power, the mass formation speed increases with powder feed rate [119].

Since the melting temperatures of many metals are relatively high, parts are heavily prone to oxidization during DLD. Therefore, inert gases, such as argon, are required to help in displacing oxygen within the DLD machine chamber and PDS. The tolerated amount of oxidization varies with application and material, but as an example, oxygen levels in the range of 2–3 ppm are typically acceptable (Griffith et al. [66]). The chamber is typically purged between 5 and 20 L per minute with a 'shielding' gas, while the PDS 'carrier' gas purge rate is governed by feed rate.

In addition to generating and repairing single-type materials, multi-nozzle DLD (LENS) can be used to generate functionally,
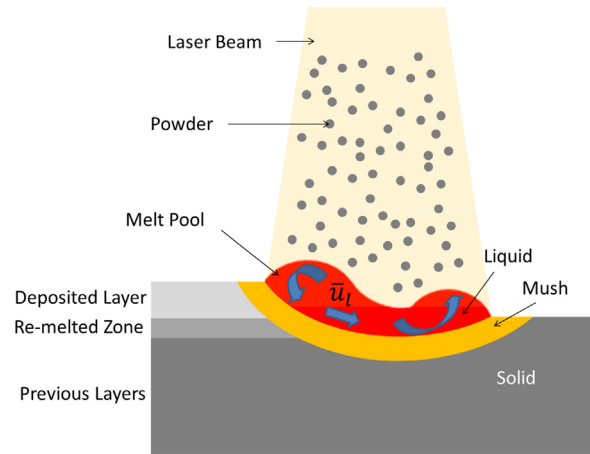
Fig. 6. Heat affected zone (HAZ) with melt pool during DLD.

compositionally graded material, such as H13 tool steel and copper for thermally conductive mold dies or implants [120–123], tungsten carbide-cobalt cermet [46], compositionally gradient titanium-chromium alloy [124,125], compositionally gradient titanium-vanadium and titanium-molybdenum alloys [126], nickel aluminides [127] and AISI 316L SS-Inconel 718 [128]. Functionally Graded Material (FGM) possesses variation in bulk properties with respect to space and this is accomplished by changing the chemical composition of the part. FGM parts are fabricated via LENS with multiple PDSs and nozzles. Griffith et al. [129] investigated using multiple powder feeders (LENS) to accomplish either graded deposition or layered deposition with combinations of AISI 316 SS and Inconel 690. Graded (heterogeneous) deposition is the process of starting with 100% of Material A at a deposition layer and then gradually transitioning to 100% of Material B. The final layer of the graded/heterogeneous part consists of 100% of Material B. Layered deposition is the alternating of materials with respect to layer. Fully dense parts were made for both graded and layered deposition methods.

Understanding, modeling and optimizing the particle/laser interactions, prior to melt pool entry, is important for furthering DLD technology. Sensible preheating and melting of the blown powder will have a direct impact on the melt pool morphology. The powder stream will attenuate the laser beam and result in thermal radiation scattering, particle-to-particle collisions and 'wasted' particles not used for the build. Modeling the powder stream dynamics can help in predicting the deposition efficiency during DLD and this can help in saving material.

3. The melt pool

The melt pool (or molten pool) is the region of superheated molten metal in proximity to the laser/material interface – typically in the form of a spherically shaped droplet that moves at the traverse speed. As shown in Fig. 6, it sits atop the HAZ and is thermodynamically unstable – adjusting in shape and in internal energy due to surrounding heat transfer and liquid/solid interactions (at wall and due to blown powder). The metallic powder is blown into it while the laser ensures its survival via energy transfer. Since the melt pool is the initiation of the solid part, its morphology, temperature and wetting behavior are of paramount interest in quality control. Dimensional tolerances and microstructural features of the finished part, as well as the existence of residual stress, depend on the melt pool behavior and shape during the DLD process. The melt pools inherent to DLD are not too different from the melt pools generated in more traditional laser and arc welding procedures; however, the continual powder/mass

addition complicates its temperature/momentum predictability and also induces free surface instability (e.g. splashing).

3.1. Boundary transport

Due to the natural limitation of thermal radiation (e.g. no true blackbody), and due to interference from the blown powder, only a portion of the incident laser is absorbed by the melt pool. This portion of heat is then either transferred sensibly to the environment via radiation/convection or sensibly/latently to the combined HAZ/melt pool region. The laser heat flux can then be estimated as [130]:

$$q''_{laser} = \frac{2\alpha_m P}{\pi R^2} \exp\left(-\frac{2r^2}{r_{b,i}^2}\right) \tag{5}$$

where P_{laser} is the laser power, $r_{b,i}$ is the radius of the laser beam at the melt pool interface, r is the radial distance from the center of the laser beam and α_m is the absorptivity of the melt pool. Note that Eq. (5) does not consider heat transfer between the laser and blown powder. At the junction of the melt pool/vapor-gas interface, the local heat loss (at location x) can be estimated as [131]:

$$q''_{loss} \cong h_x(T(x) - T_\infty) + \varepsilon\sigma(T^4(x) - T_\infty^4) + \rho_L\left|\frac{\Delta x}{\Delta t}\right|_e h_{LV} \tag{6}$$

where the first term on the right-hand-side (RHS) of Eq. (6) corresponds to heat loss due to Newtonian convection with the adjoining purge gas, at temperature, T_∞, as described by a local heat transfer coefficient, h_x, and local surface temperature, $T(x)$. The second RHS term corresponds to net radiation with the purge chamber assuming gray-surface radiative behavior with ε being the melt pool emissivity and σ being Stefan–Boltzmann's constant (5.67×10^{-8} W/m^2 K^4). In approximating the net radiation between the melt pool surface with the purge chamber, it is important to realize that many idealizations are made. For example, the melt pool surface is assumed to be a graybody – implying that the net radiation transfer is wavelength independent and that the surface emissivity is near-equal to its absorptivity. The gas temperature can also be assumed to be near-equivalent to the chamber wall temperature. The third RHS term corresponds to heat loss due vaporization of the melt pool and ρ_L is the density of the liquid, $\left|\frac{\Delta x}{\Delta t}\right|_e$, is the rate of melt pool topology deformation due to evaporation and h_{LV} is the latent heat of vaporization. The melt pool topology deformation rate can be estimated using [131]:

$$\left|\frac{\Delta x}{\Delta t}\right|_e = c_s \exp[-\bar{h}_{LV}/T(x)] \tag{7}$$

where c_s is the speed of sound in the melt pool and $\bar{h}_{LV}$ is latent heat of vaporization per unit atom. Vapor recoil, or boiling, in the melt pool, and convection heat transfer along the melt pool surface, can further contribute to the melt pool topology deformation [88]. The supplied heat flux, which contributes to melt pool formation, and the sensible heating of melt pool and part, is then found as: $q'' \cong q''_{laser} - q''_{loss}$. This 'useful' heat flux, q'', will also conduct through the previously deposited layers of the part and exchange heat with surroundings as it conducts to the bottom substrate. This post-melt-pool heat transfer is similar to the conjugate heat transfer found in extended surfaces (fins). The useful heat flux will depend on the laser/melt pool heat transfer significantly. The emissivity and absorptivity, as well as the reflectivity and transmissivity, of the melt pool will change with temperature, vary with radial location (due to localized irradiation and Gaussian intensity of beam) and are wavelength/material dependent. By conservation of energy, the incident thermal radiation, after traveling through the powder metal cloud, can take part in either being absorbed, reflected and/or transmitted through the melt pool.
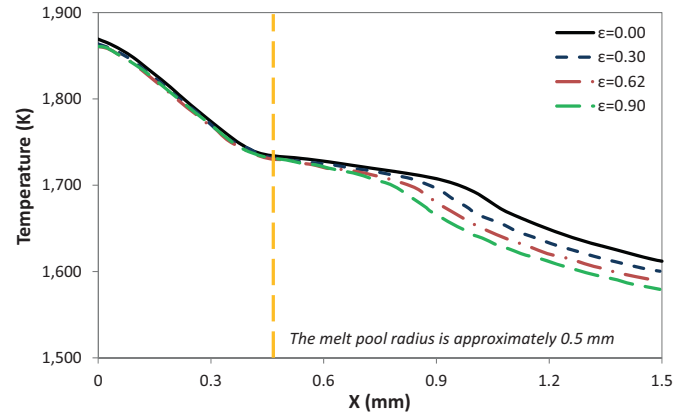

Fig. 7. Simulated temperature variation along plane of deposition for LENS as function of melt pool emissivity. The center of the melt pool is at $x = 0$ mm and approximate melt pool radius is provided [132].

Heat transfer between the melt pool and surroundings (e.g. the DLD machine chamber) is accomplished through convection with the shielding/carrier gas and thermal radiation with surrounding bodies. Radiation heat transfer during DLD is dictated by the melt pool's spectral emissivity which is a function of its superheat and amount of oxygen within/atop it. Wang and Felicelli demonstrated that the melt pool length and temperature profile are sensitive to changes in the melt pool emissivity as shown in Fig. 7 [132]. In Fig. 7, the temperature variation along the substrate is shown in addition with the approximate melt pool length. In general, as the melt pool emissivity decreases, the temperature variation along substrate length becomes more isothermal with a melt pool leading edge/boundary of higher average temperature. It was found that the overall melt pool area does not change substantially as melt pool emission changes; hence, a near-constant melt pool length of approximately 1 mm was assumed. For LENS of stainless steel, the heat loss due to convection and radiation can be on-the-order of 10% [132]. The gas flow speed in the vicinity of the melt pool can be around 30 m/s with a heat transfer coefficient on-the-order of 10 W/m^2 K [132,133]. For a given purge rate, as the operating temperature of the deposition layer increases, the heat transfer due to convection will increase [131].

Griffith et al. found that smaller particle sizes (−325 mesh) result in a more stable melt pool for Inconel 625 during DLD [66]. Larger particles with a wider range of sizes (−80 to +325 mesh) were found to provide for an unstable melt pool that was highly agitated – confirming the occurrence of free surface instability. The agitated motion of the melt pool was attributed to the larger momentum inherent to the larger particles – resulting in larger displacements in the melt pool and thus oscillations along the free surface. For minimal layer idle time, particle catching (powder efficiency) of the melt pool was found to increase with deposition layer for the build of a thin-wall structure of AISI 4340, and that the temperature and thickness of the deposits increase with each layer [134]. High powder feed rates can also result in splashing and coining of the deposition heads [135].

3.2. Temperature distribution

There will be a power-dependent temperature gradient across the thickness and radius of the melt pool due to sensible heat transfer. Since the heat transfer within the melt pool is predominantly latent, due to phase change (melting), the temperature distribution is at-or-exceeding the liquidus temperature of the material. The thermal gradient across the melt pool width/radius is significant, ranging between 100 and 1000 K/mm [13,32,40,88,97]. This is
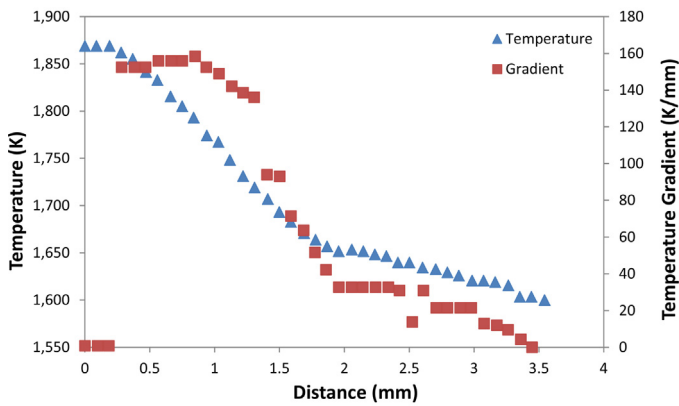
Fig. 8. Characteristic temperature distribution and gradient along the length/radius of a H13 tool steel melt pool during LENS [13].

Fig. 9. Relative temperature profile along the plane of deposition where the laser is moving left to right and the melt pool leading edge is located at approximately 6 mm [13].

attributed to the high heat flux, as the heated boundary is spatially small relative to entire melt pool. For example, maximum/peak temperatures within a melt pool of AISI 316 SS can be around 2300 K which is about 40% above its melting temperature of 1673 K, while melt pool temperatures in single-line clads of Ni20 were found to have temperatures 30% higher than their liquids [33,115]. The powder injection affects the melt pool superheat [136], and increasing the powder feed rate will decrease the melt pool temperature [33]. In addition, the center-axis of the blown powder, or relative positioning of the powder nozzles to the center of the melt pool, will impact the melt pool temperature and its temperature profile [33]. Griffith et al. demonstrated the high superheat and temperature variation along the DLD-inherent melt pool via infrared thermography of LENS processing of AISI 316 SS and H13 tool steel [13,40].

As shown by Griffith et al., and specifically for a LENS-build of a H13 tool steel thin-wall, the maximum melt pool temperature is located near the laser and is noticeably higher than the melting temperature (1700 K) of the processed material (e.g. superheat) [13]. As shown in Fig. 8, a near-Gaussian temperature profile exists in the melt pool with high-ordered variation near the laser location and more linear variation toward the trailing edge of the melt pool ($x = 0$ is leading edge). The linear variation within the trailing edge region can be attributed to solidification heat transfer and pool-to-surroundings heat transfer. The high-ordered variation can be attributed to superheat-driven, sensible heat transfer effects near the high heat flux laser/pool interface. In the solidifying region, the gradient is non-constant and decreasing with location from the melt pool center, while in the laser heating zone, the gradient is near-constant due to the phase-change heat transfer. It may be seen that the temperature gradient along the melt pool is very steep across its leading edge – on-the-order of 150 K/mm. In fact, it was found that the maximum thermal gradient (160 K/mm) was off-set from the center heating location. At the center of heating, the axial temperature gradient is effectively zero, but then approximately 0.25 mm from the center heating location, is on-the-order of 150 K/mm – where it remains near constant throughout the superheated liquid which has a length of approximately 1.25 mm. The gradient then decreases rapidly near the trailing edge of the liquid region to approximately 30 K/mm during solidification heat transfer [13]. For AISI 316 SS, Ye et al. [32] numerically determined a temperature gradient on-the-order of 500 K/mm in vicinity of the melt pool, confirming initial, experimental measurements reported between 200 K/mm and 400 K/mm [97]. For ceramic-based metals, the temperature gradients near the melt pool can be very high. For example, the DLD of tungsten carbide-cobalt can have thermal gradients near 2000 K/mm [46].
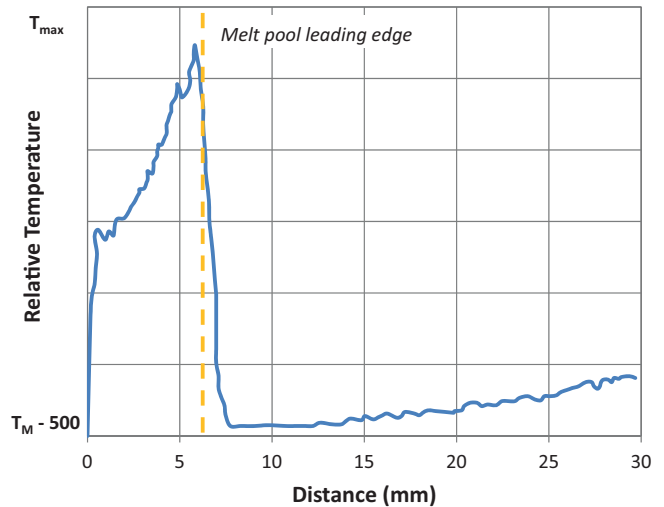
Via infrared thermography, Griffith et al. also characterized the temperature gradients inherent to the melt pool region on a AISI 316 SS part during DLD [13]. 'Relative temperatures' were measured to indirectly determine the absolute temperature of the part during LENS without a priori knowledge of its emissivity. A representative temperature profile along a plane undergoing deposition is shown in Fig. 9. A steep temperature gradient of approximately 500 K/mm is observed near the leading edge of the melt pool which is traveling left-to-right. Integrated, long time-scale heating effects are also observed, as the end-point of a previous deposited layer possesses a higher temperature than the temperature in which the melt pool is advancing toward. It can be seen that the melt pool, with ~5 mm length, has significant temperature variation, with a radial temperature gradient on-the-order of 50 K/mm.

Wang et al, using pyrometry during the DLD of a thin wall of stainless steel, demonstrated that the temperature distribution within the melt pool is sensitive to laser input power and is, for majority of laser powers investigated, superheated above the liquidus temperature [34]. The melt pool temperature distribution becomes more isothermal as the laser power decreases, while its peak temperature increases with higher specific energies (slower traverse speeds and higher laser powers). Furthermore, the maximum temperature of the melt pool varies with layer number during fabrication of the part and, in general, asymptotically decreases in value as the layer number (or part height) increases [101]. The melt pool/gas heat transfer coefficient can also impact the temperature profile of the melt pool. As shown in Fig. 10, higher heat transfer coefficients ($h \sim 500$ W/m^{2}K) can alter the temperature profile so it decreases much more rapidly – achieving lower temperatures at all points in space [132]. These trends indicate that forced convection can be used for melt pool temperature control; while also demonstrating that the purged chamber environment for a typical DLD machine, which can consist of mixed free/forced convection ($h < 100$ W/m^{2}K), is conducive for achieving isothermal melt pools. Melt pool surfaces with less temperature variation can be easier to monitor via pyrometry, since steep temperature gradients are harder to resolve.

Tang and Landers, using single-nozzle DLD for H13 tool steel – found that the average melt pool temperature was around 2140 K [35]. This average temperature varied slightly as the process parameters (e.g. laser power, traverse speed and powder feed rate) were varied. The melt pool transient response, as quantified by a thermal time constant, was experimentally measured by altering the
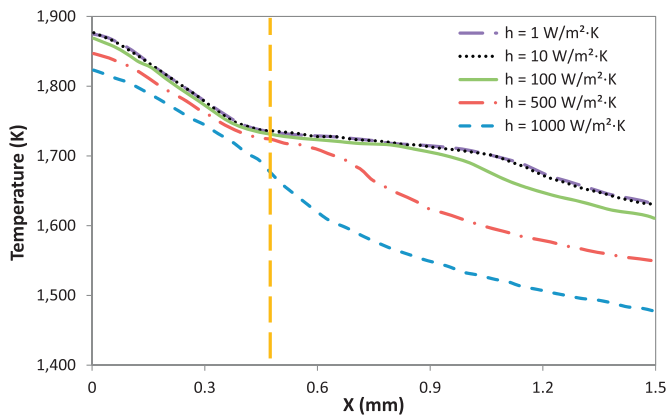
Fig. 10. Simulated temperature variation along plane of deposition for LENS as function of heat transfer coefficient. The center of the melt pool is at $x = 0$ mm and approximate melt pool radius is provided [132].

process parameters and was found to be on-the-order of 30 ms. Due to bulk heating effects, subsequent layers, and traverse deposits (along the track) were shown to have a melt pool with higher temperature while the laser power was held constant. For constant laser power, heat accumulation can occur as more layers are deposited on the part and little-to-no inter-layer idling is utilized. This heat accumulation, which also depends on the heat transfer with surroundings and substrate material/dimension, will impact the initial temperature of the melt pool along a new deposition path. In a limiting case, it is possible for the initial temperature of a new layer to approach the final temperature of the last-deposited layer – thus supporting heat accumulation. In addition to impacting the melt pool temperature, heat accumulation can result in secondary, microstructural evolution in solidified regions of the DLD part and this can complicate any process control. Furthermore, although the melt pool temperature, if actively monitored, can be used as part of a closed-loop feedback control system in order to adjust laser irradiance and other input parameters in real-time [66], it has been demonstrated that controlling a constant melt pool temperature for a given location does not necessarily generate a uniform track morphology [137]. Such methods for thermal control during DLD are discussed in detail within Part II.

The melt pool temperature/morphology is affected by interfacial forces such as surface tension and metal vapor recoil – with recoil vapor pressure being more prevalent at and beneath the melt pool center [131,138]. The highest superheat will be directly below the melt pool, in the center of the HAZ, and this can initiate boiling heat transfer (or vapor recoil) characterized by the birth/growth of metal vapor bubbles and trapped inert gas. When the vapor recoil force exceeds the liquid/gas surface tension force near the periphery of the melt pool, the melt pool is expulsed. The recoil force increases with temperature faster than the surface tension force, therefore, as the process parameters are varied as to increase the bulk temperature near the melt pool, mass loss due to boiling in the melt pool is possible. The tendency for liquid metal expulsion to occur, due to vapor recoil forces, will increase as the irradiated power intensity increases [138]. The vapor recoil force, F_r, can be estimated as:

$$F_r = 2\pi \int_0^{r_B} r \Delta P(r) dr \qquad (8)$$

where T_{sat} is the vaporization temperature of the metal at atmospheric pressure, r_B is the radial distance in which the surface temperature reaches T_{sat} and $\Delta P(r)$ is the radial variation in vapor pressure. Heat loss due to vaporization of the melt pool can also occur and be somewhat detrimental to DLD. However, as the laser power increases, the effects of vapor output from the melt pool

actually decrease due to increased plasma pressure above the melt pool region [112].

Marangoni convection, which is fluid motion driven by surface tension gradients, can increase the natural convection heat transfer in the melt pool, by increasing advection along the periphery. This mechanism provides for transport of thermal energy from the center of the laser beam to the melt pool periphery via convection; with radial temperature gradients exceeding those of depth-wise temperature gradients [139]. This indicates that melt pool heat transfer (and temperature distribution) is coupled with its morphology which is also coupled with the wetting behavior at the part interface. The Marangoni-type heat transfer in 'surface-tense' melt pools is in contrast to the free convection heat transfer inherent to melt pools with low surface tension. Marangoni transport supports free convection flows and thus provides for higher peak velocities in the melt pool and higher intra-pool heat transfer coefficients. With negligible Marangoni transport, free convection flow dominates, but the peak velocities are much smaller and the heat transfer through this type of melt pool can be estimated via conduction alone [139].

For fluids with highly temperature-sensitive surface tensions (N/m/K), γ, Marangoni transport can dominate and result in a shallower melt pool with altered solidification behavior due to increased heat transfer and fluid flow along its periphery. For a given temperature difference, such fluids can solidify to form taller clad/track heights [140]. Lee et al. indicate that Marangoni convection is concentrated near the tail of the melt pool boundary – as evidenced by a relatively flat temperature profile in that region [105]. When both Marangoni convection and vaporization coexist within a melt pool, the melt pool free surface temperature distribution and its peak value are significantly affected by the surface tension dependence on temperature [141].

3.3. Fluid dynamics

During DLD, strong temperature variation along the melt pool results in both density and surface tension gradients along its length/thickness, driving both free convective and Marangoni-type flows within itself, respectively [139,141–143]. Secondary and tertiary thermocapillary-type forces – driven by contact angle variation along deposited layers – as well as disjoining pressure effects will also contribute to melt pool internal fluid dynamics. Powder feed rate and particle angle-of-attacks will significantly affect the free surface stability and motion of the melt pool, as well. All of these forces/gradients will affect the melt pool free surface and its internal fluid motion. Thus, the melt pool momentum will impact its morphology, as well as the post-melt pool track integrity/shape and heat transfer to and through the part. For a given laser power, metallic fluids with high surface tension sensitivity to temperature will tend to have higher peak velocities within its melt pool during DLD, with characteristic peak velocities on-the-order of 1 m/s [101,139,142]. The peak velocity will increase with laser power for a given focal area; hence, the temperature difference between the irradiated top surface of the melt pool and its periphery will most likely increase [144,145] and this will drive stronger convection currents with higher peak velocities. As the specific energy delivered to the melt pool decreases (lower laser power, higher traverse/scan speeds), its peak temperature should decrease, and buoyancy-driven/surface-tension driven flows will have slower peak velocities. In special cases, the fluid velocity inside the melt pool can achieve velocities higher than the traverse speed by approximately 50–70% [115].

Maximum velocities occur in the region of the free surface of the melt pool concentrated near steep temperature gradients and are slightly lower for metals with a positive surface tension coefficient (as opposed to negative surface tension coefficients) [142].

Metals with negative surface tension coefficients will have buoyancy and surface tension forces that reinforce one another and thus provide for faster flows. Melt pool flow direction at the surface, governed by Marangoni convection, will flow in a direction as dictated by the surface tension-temperature sensitivity (surface tension coefficient), $\partial\sigma/\partial T$. The surface tension coefficient of pure metals is negative; however, the addition/presence of impurities (or alloys) can cause the dependence to become positive and reverse the direction of fluid flow within the melt pool [142].

For melt pools initiated by gas-tungsten-arc (GTA) welding, where the temperature variation within the HAZ can be substantially less than DLD, evidence of turbulent melt pool fluid flows have been demonstrated [146]. Turbulence modeling within a melt pool undergoing high laser power transfer and solidification can then be accomplished using the $k-\varepsilon$ Reynolds-Averaged Navier–Stokes (RANS) method through Computational Fluid Dynamics (CFD) [147]. Through turbulence modeling, it can be observed that diffusive effects related to turbulence can significantly affect the solute and momentum transport in the melt pool while also increasing the convective heat transfer, but this thermal enhancement is not very significant. Second-law analysis was performed by Chatterjee and Chakraborty to model the entropy generation and turbulent transport in a melt pool during laser surface irradiation, and it was found that the melt pool energetic and exergetic efficiencies are not sensitive to powder feed rate, but increase with higher laser powers [148]. The exergetic efficiency was found to decrease with traverse speed – indicating better thermodynamic utilization during faster traverse speeds. Their study concluded that the majority of entropy generation is attributed to heat transfer through the melt pool, while fluid flow and mass transfer contribute only a small portion toward total entropy generation.

As the melt pool region becomes deeper (penetration depth increases), melt pool vorticity increases – with a three-dimensional, 'swirl'-type flow becoming more prevalent – indicating higher turbulence [149]. Lei et al. demonstrated that when surface tension gradients are small within the melt pool, evaporation heat loss from the melt pool becomes non-negligible and can reduce its peak temperature [141]. They also demonstrated that very large surface tension gradients in the melt pool will decrease the influence of vaporization heat loss on the peak temperature and shape of the melt pool. Negative surface tension/temperature sensitivity (gradient) along the melt pool is indicative of a melt pool with a wide and shallow shape with flow occurring outward, toward the periphery of the melt pool. Positive surface tension/temperature sensitivity is indicative of a melt pool with a narrow and shallow shape with flow occurring inward toward the center of the melt pool [141]. The melt pool can also have a three-vortex flow pattern during track deposition [115]. For positive Marangoni numbers, $Ma \sim \gamma\Delta h_{ls}$, with Δh_{ls} being the difference in specific enthalpy of fusion at liquidus and ambient temperatures, the finest grains are formed closer to the bottom of the melt pool, while negative Marangoni numbers result in melt pools generating finer grain structures along the top of a layer [140].

The wetting behavior, which describes the liquid/surface interaction and droplet morphology, and free-surface stability of the melt pool, can be predicted via use of pseudo-steady-state contact angles and the Bond and Froude numbers, respectively. The contact angle along the melt pool three-phase interline, θ_{eff}, must have surface tension forces that balance according to Laplace-Young's equation, i.e.:

$$\sigma_{SV} + \sigma_{SL} = \sigma_{LV}\cos\theta_{eff} \qquad (9)$$

where σ_{SV} is the surface/vapor surface tension, σ_{SL} is the surface/liquid surface tension and σ_{LV} is the liquid/vapor surface tension. The Bond number is predictive of the melt pool shape based on surface tension and gravitational forces, while the Froude

number can be used to predict waves atop the fluidic interface. Defining the Froude number as $Fr = v_p^2/gd_p$, with v_p, g and d_p being the powder velocity, local acceleration due to gravity and particle diameter; a 'stable' meniscus, undergoing a 'smooth' deposition process with no splashing or waves would then be characterized with $Fr < 1$ [81].

3.4. Morphology

The geometry of a deposition track is dictated by it's fluidic behavior and solidification rate. The profile of the deposition layer is limited by the morphology/wetting behavior of the melt pool, and limiting profiles can be estimated based on the surface tension and contact angle within the melt pool [103]. A discussion of melt pool morphology then includes a discussion on post-melt-pool track morphology.

The melt pool free surface topology, or interline morphology, is highly transient due to blown powder entry, gas flow, oxidization and laser irradiation. This morphology is then further coupled with surface/fluid phenomena such as surface tension, capillary forces and the melt pool fluid dynamics [109]. Since the melt pool is the initiation of the part, its morphology is of interest and indicative of the process effectiveness, as a consistent melt pool size is a strong indicator of part quality. The melt pool shape depends on many variables during DLD. For example, the blown powder efficiency, liquid/solid wetting behavior, inert gas flow rates, heat transfer and more.

Peng et al. [113] investigated the effect of specific energy on the morphology/shape of a melt pool atop nickel alloy during DLD. It was demonstrated that, in general, as the specific energy increases, the deposition layer height, width and depth increase. There is a critical specific energy in which inflection in these trends occurs and for nickel alloy is around 300 J/mm². Also, when the ratio of the deposition depth (into part) to part thickness becomes too large, then previously deposited layers can re-melt. Too small a ratio results in less adhesion between adjacent layers [113]. Others have found that increasing the powder feed rate decreases the depth of melt pool [112] while there is a positive linear relationship between layer thickness and the input specific energy for a given (single-nozzle) powder feed rate [72].

The melt pool shape strongly depends on the traverse speed. Wang et al. numerically demonstrated that the melt pool becomes elongated at higher travel speeds and penetrates less into successive layers – thus impacting the HAZ [150]. The melt pool length and temperature increases with laser power or slower traverse speeds [33], while the cooling rate at the liquid/solid interface decreases [132]. They also demonstrated that higher substrate temperatures correspond to longer melt pools with little effect on the temperature profile. The melt pool length decreases as the gas heat transfer coefficient increases to atypical DLD values (e.g. $h > 500$ W/m² K), but remains near constant for more-feasible DLD process heat transfer coefficients, e.g. $h < 100$ W/m² K [132]. The melt pool length can range between 0.5 mm to 1.5 mm for the LENS processing of tool and stainless steels [133] and typically increases in length with layer number [34]. The melt pool aspect (e.g. length-to-width) ratio increases near-linearly with traverse speed and laser power. Typical aspect ratios for a melt pool for single-nozzle DLD of AISI 316L stainless steel can range between 1.0 and 1.5 [103]. Layer height and width increases with the laser power, while the deposition layer height increases with the material flux to the melt pool [103].

Although the melt pool will elongate as the traverse speed increases [103], the depth of the melt pool will decrease [112]. However, others have shown only slight dependence of the melt pool depth with traverse speed [34]. Interestingly, the melt pool depth can be non-unique for various traverse speeds, meaning, for a given (constant) laser power and powder feed rate, a specific melt

pool depth can be achieved with two traverse speeds – and this is attributed to the parabolic dependence of melt pool depth on traverse speed [151]. Raghavan et al. [38] demonstrated that the aerial profile of the melt pool alone is not an indicator of overall morphology, as the depth and overall volume, can be significantly different. The build height was shown to depend linearly on number of passes [152].

The scan width can be controlled by altering the beam diameter with a lens. This will control the imposed heat flux at the deposition layer interface. Pi et al. found that the cross-sectional morphology (build height/profile) of AISI 316 SS (single nozzle) depends strongly on the scan width [42]. Keeping the laser power constant, while decreasing the scan width, results in a single-line morphology with an arc-shaped top, and this arc becomes more exaggerated with subsequent deposition layers. This arc-shaped morphology can eventually lead to the collapse of the part wall, since the melt pool can run off the inclined surface. Higher powder feed rates can result in a deposited layer having a width greater than that of the melt pool at the surface of the substrate [103].

Pinkerton and Li demonstrated that the top layers of a single-layer-width (thin) wall obtain more of a circular profile as opposed to elliptical, flat profiles [103]. Top layers, due to bulk heating of the part, may have more hydrophilic melt pools which can result in the so-called 'mushroom effect' – meaning, such layers will be wider in shape then the previously deposited layers [107]. For such parallel-line scanning, the deposition head must accelerate or decelerate at the beginning and end of each deposition trail (or trace), respectively. For constant laser power and powder feed rate, this results in an observable phenomena known as a 'step effect' which becomes more prominent with layer number [42,153]. Basically, the trace will have a hump, or nodulation, at its start and end.

Thompson and Szekely [142] indicate that a melt pool with a higher characteristic surface tension will have a similar width, narrower depth and a higher maximum penetration depth relative to melt pools with lower surface tensions. For positive surface tension coefficients, the convection heat transfer is concentrated downward, near the centerline of the melt pool – creating a deep penetration; however, when the coefficient is negative, convection heat transfer is concentrated near the melt pool free surface – resulting in a wider melt pool region [142].

The free surface of the melt pool will dictate the deposited layer cross-sectional profile. This liquid/vapor interface (or melt pool/vapor-gas mixture interface) is unstable and in non-equilibrium – given the blown powder mass addition, heat transfer, fluidic motion and previous layer surface roughness/surface quality. The powder injection actually results in a tilted melt pool profile, as shown in Fig. 6, and the angle of this tilt is related to the deposition layer thickness and melt pool length [136]. For multi-track deposition, the morphology of the melt pool becomes more asymmetric in shape, becoming more 'tilted', relative to single deposition [154]. For secondary adjacent track deposits, the melt pool now leans on a side deposition wall and the convective area and wetting behavior are altered. Multi-track deposition is also susceptible to adjacent and bottom layer re-melting [154]. Furthermore, the number of nozzles utilized to accomplish DLD will impact the topology of the melt pool, and the tilt angle will become more axi-symmetrical. The morphology, or free surface, of the dynamic melt pool can be modeled using level set theory [101,109,130]. The morphology can also be assumed using the liquidus isotherm [88].

4. Solidification

Solidification of the melt pool is governed by the net heat transfer through the melt pool and can be classified into three major events: (1) heterogeneous nucleation, (2) mushy-zone heat/mass transfer and (3) microstructural evolution via heat treatment. As shown in Fig. 6, the mushy zone is the region between the melt pool and the solid material. It supersedes or is co-located with the HAZ. The mushy zone is a two-phase mixture – with remnants of solid particulate and molten metal. Natural convection is the means of heat transfer in the mushy zone, as the density variation is significant. The mushy zone is a result of melting and solidification occurring over a finite temperature range over a spatial domain – as observed by the coexistence of liquid and solid metal. This temperature range is in between the solidus and liquidus temperature. This mushy zone behaves as a porous medium – dampening the liquid momentum [131] and can be modeled as having a permeability.

The phase-change heat transfer and momentum at the solid/liquid boundary of the melt pool is perhaps the most technically sophisticated physical process inherent to powder-based DLD. The blown powder mass addition contributes to melt pool instability and transient morphology; while the trailing edge of the melt pool gives its latent heat of fusion to form the solid deposited layer. This complex diffusion process is further coupled with the temperature-dependent microstructure evolution that depends strongly on material type. Solidification for carbon steels is different than that of Ti-6Al-4V and this is due to the various chemical elements in the alloy. Microstructural evolution describes the initiation and growth of grain boundaries, or solidification interfaces that can either be columnar, planar or dendritic. Marangoni convection can impact the solidification heat transfer, as well. For instance, Yin et al. demonstrated that no significant macro-segregation is evident during DLD-based solidification of SS410 and this was attributed to Marangoni-type mixing effects [139]. For relatively high traverse speeds, dendrite-to-cellular transition was observed during the DLD simulation of steel (Fe−0.13wt%C) [155]. Surface tension will impact the solidification heat transfer, with higher surface tension metals providing for higher melting rates along the melt pool centerline [142].

Porosity can exist in the DLD-fabricated part and can be attributed to inefficient solidification mechanisms or the existence of parasitic phenomena such as entrapped gas or debris. Lack of effective fusion between successive layers can result in the existence of porosity and can occur due to lack of sufficient laser power, typically at the beginning of a track deposition since this region has undergone more cooling relative to other regions [102]. Un-melted particles can affect the porosity, as well – and are more likely to be present in the first/second deposition layers near the substrate due to the large amount of heat traveling to the substrate in the early phases of DLD. For the DLD of functionally graded parts, different material powders can be added to the melt pool simultaneously. For this type of DLD, it has been found that imposing a negative enthalpy of mixing results in more homogeneous intermixing in the melt pool accompanied with a rapid rate of solidification [124].

The cooling rate is the temperature change of the melt pool with respect to time and varies along the volume of the melt pool; being the highest at the solid-liquid interface and decreasing with distance from the center of the melt pool [153]. It will depend on the heat loss and conduction heat transfer through part. The melt pool cools very rapidly since the melting temperature of a metal is almost two orders-of-magnitude higher than that of the surrounding inert gas and environment. This can be advantageous in producing very fine grain structures and thus desirable mechanical properties [129]. The cooling rate, at a given location near the melt pool, can be found by multiplying the temperature gradient at the liquidus isotherm, $\nabla T_l(r, t)$, with the traverse speed, V_{beam}, e.g.:

$$\frac{\partial T}{\partial t} \cong \left\| \nabla T_l(\boldsymbol{r}, t) \right\| \cdot V_{beam} \tag{10}$$

An empirical form for the cooling rate can be used to help in estimating the solidification heat transfer. Zheng et al. suggested a correlation, e.g.: $\lambda_2 = A(C_R)^{-n}$, where λ_2 is the dendrite arm spacing

(DAS) – on-the-order of micrometers – C_R is the cooling rate, and A and n are material constants [50].

The melting efficiency, η_{melt}, can be defined as the ratio of energy utilized for melt pool formation over the total heat generated from the heat source for a given instant in time and can be correlated with non-dimensional groups such as the Christensen and Rykalin numbers, shown in Eqs. (12) and (13), respectively [106].

$$\eta_{melt} \approx \frac{Ch}{Ry} = \frac{V_{beam} A_m \Delta H_m}{\eta_a P} \tag{11}$$

where

$$Ch = \frac{V_{beam}^2 A_m}{\alpha^2} \tag{12}$$

$$Ry = \frac{\eta_a P V_{beam}}{\alpha^2 h_{LS}} \tag{13}$$

where η_a is the energy efficiency, P is the laser supply power, α is the thermal diffusivity of the metal at liquidus temperature, h_{LS} is the latent heat of fusion and A_m is the melt pool cross-sectional area. This demonstrates that the melting efficiency is predictable given the process parameters and thermophysical properties of the metal. Melting efficiency of LENS H13 tool steel was shown to increase as the powder feed rate, traverse speed and laser input power increased [106].

Simchi [114] demonstrated that the densification of ferrous metal powders, D, can be expressed as a function of the laser specific energy as: $-\kappa E = \ln(1 - D)$, where κ is the densification coefficient and depends on the part material (chemical composition), particle size and the oxygen content within the blown powder. It was also shown that the densification rate of high-alloy steels, such as AISI 316L SS, is higher than that of ferrous and low-alloy powders for a given set of process parameters. The densification rate for finer powders is higher than that of coarser powders, as well.

Predicting the microstructures inherent to solidification requires modeling the nucleation and growth of all possible phases. As the melt pool solidifies – the previously deposited layers, or bulk region of the part and substrate (i.e. far from HAZ) behave as a heat sink and this results in directional solidification [88]. The grains, or solid-phase columnar fronts – move in a direction opposite to the heat flux vector at a specific velocity. For surface laser processing, a relation between the melt pool thermal gradient, G, and solidification velocity, V_{iso} is provided as:

$$\frac{G^{3.4}}{V_{iso}} \approx 8113 \left[\sqrt[3]{\frac{-4\pi N_o}{3\ln(1-\varphi)}} \right]^{3.4} \tag{14}$$

where N_o is the number of nucleation sites and φ is the volume fraction of equiaxed grains. This ratio, namely $\frac{G^{3.4}}{V_{iso}}$, is a strong indicator of microstructure evolutionary phases and should be controlled in all locations of the melt pool to ensure uniformity in microstructure. The number of nucleation sites for solidification will change depending on whether DLD is being utilized for repair or for AM – as the surface condition/roughness will be important. The solidification velocity is related to the laser travel velocity and melt pool morphology [88], and the melt pool thermal gradient is dictated by the laser power and established temperature field in the part/substrate. Since the thermal gradients are high for laser processing, the exact position of liquid/solid interfaces – or dendrite tips – can be neglected. In this case, the solidification velocity can be approximated as the advancement rate of the liquidus isotherms, V_{iso}. This solidification velocity can be related to the laser travel speed by:

$$\left| V_{iso} \right| = \left| V_{beam} \right| \cdot \cos\theta \tag{15}$$

where θ is the angle between the solidification front's unit normal vector and the laser beam moving direction [88]. The solidification
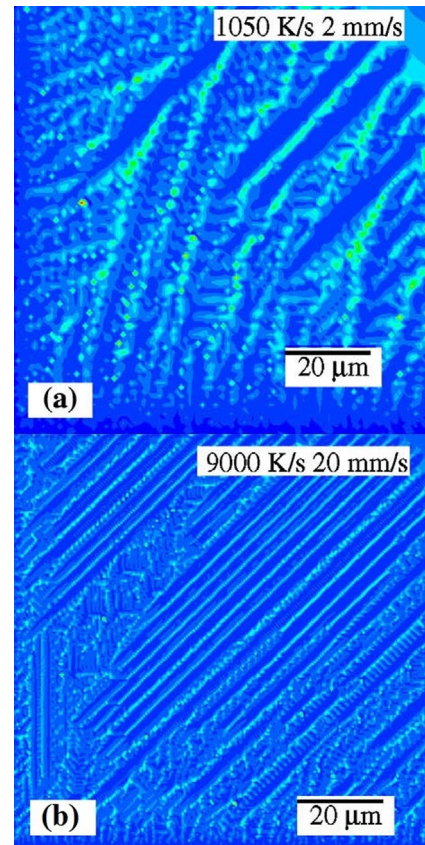

Fig. 11. Effect of traverse speed on the simulated HAZ-vicinity cooling rate and microstructure of a carbon-based steel (a) traverse speed = 2 mm/s (b) traverse speed = 20 mm/s [158].

velocity ranges from near zero at the bottom and sides of the melt pool to a maximum value near V_{beam} at the trailing edge of the melt pool [156]. Variations in the melt pool shape due to powder addition and surface wetting will affect dendritic growth direction and can also affect the solidification velocity [88]. The strong thermal gradients in the melt pool give rise to natural convective flows that can be turbulent in scale and thus impact solidification – especially the mechanisms for nucleation. Un-melted powders will behave as nucleation sites within the solidifying melt pool, thus the powder melting efficiency will directly impact the solidification and microstructure.

The observed microstructures within a part fabricated via DLD will be informative of the solidification heat flux vector direction during DLD. For instance, the presence of directional columnar microstructure is indicative of unidirectional heat flux in the height-wise direction (e.g. for non-complex, rod/thin-wall structures) [50,157] – such a heat flux suggests that the transient conduction heat transfer through the part is primarily one-dimensional – occurring from the melt pool to the substrate.

The crystalline/dendritic morphology depends strongly on the cooling rates experienced during DLD. In general, higher cooling rates lead to finer microstructures, or in other words, dendritic morphology characterized with low DAS. Dendritic arm spacings are on the order of 1–10 μm and depend on the DLD process parameters and material used [158]. The solidification for various carbon-steels undergoing DLD was simulated using the cellular automation (CA) method and it was shown that the DAS decreases as the cooling rate increases [158]. It was further shown that as the traverse speed decreases, the dwell time of the heat source on the deposition layer increases – decreasing the cooling rate and solidification velocity. As shown in Fig. 11, increasing the traverse speed increases the

cooling rate which results in a microstructure with a lower characteristic DAS and the introduction of cellular-type growth [158]. The simulation also corroborates experimental results by indicating that the cooling rate decreases as the powder feed rate increases – creating thicker deposit layers and larger melt pools that have higher latent heat transfer and smaller thermal gradients (and less cooling). Larger melt pools are conducive for grain evolution as they have more time to grow. A DLD process that provides for low power and smaller melt pools will result in smaller-DAS, finer micro-structural parts [97,158]

Typical cooling rates for a thin wall of LENS deposited stainless steel can vary between 1000 °C/s to 6000 °C/s [34] with peak cooling rates on-the-order of 12,000 °C/s [150] – in agreement with original, experimental measurements estimating between 100 K/s – 1000 K/s [97]. The maximum cooling rate increases, and the trailing-edge cooling rate (at tail of melt pool) decreases, with higher traverse speeds, while both decrease and increase with laser power, respectively [33]. The highest cooling rates occur in the liquid ahead of the liquid/solid interface [97] for lower powers and higher traverse speeds; however, this maximum cooling rate typically decreases with deposition layer number (e.g. as the part gets taller) [150]. Peak cooling rates are short-lived for most DLD processes – being sustained for time frames on-the-order of a couple of seconds. For instance, the temperature can decrease from 2000 °C to 100 °C in 2 s for the first layer of deposition of stainless steel [150]. Due to this short time scale for cooling, the idle time between successive deposition layers – inherent to the DLD process – is frequently sufficient for effective layer-to-layer adhesion.

Via thermography, the temperature time rate of change near the mushy zone and melt pool has been estimated to be on the order of 100–1000 K/s, for stainless and tool steels during the LENS process [133]. These cooling rates, when compared to other metal solidification processes in manufacturing, and while considering the length-scale associated with DLD, are similar. It has also been demonstrated that the cooling rate increases as the deposition layer thickness and/or specific energy decreases [72], while others indicate that the solidification rate (or quenching rate) decreases [50]. This indicates the presence of 'exposed' and 'intra' cooling rates being non-equal during DLD – especially as the deposition layer thickness increases.

Solidification may be modeled by using mixed thermophysical properties (e.g. density, isobaric specific heat, latent heat of fusion, thermal conductivity, etc.) weighted by volume or mass percentage within the conservation equations for mass, energy and momentum [131]. Solidification simulation can be approached in many different ways [98] as the modeler can either take a microscopic or macroscopic approach. In the macroscopic approach, the heat and mass conservation equations are solved via finite difference/elemental methods. In such macroscopic approaches, the mushy zone is highly simplified [98]. It is with a microscopic approach that more detail in solidification modeling arises; but at the cost of computational power. Nucleate solidification can be modeled using a continuous Gaussian nucleation distribution – which can estimate how grain density changes with undercooling, while a probability for nucleation within a finite or differential volume can also be defined [155,159].

Kelly and Kampe [160] numerically investigated the coupling of thermal history with microstructural evolution during the 8-layer single-line deposition of titanium alloy (Ti-6Al-4V). It was found that as the traverse speed decreases, and the elevation (z-position) within a layer increases, the peak temperature increases – while there is little effect on cooling rate [160]. It was also found that the initial cooling rate in a newly deposited layer decreases as the deposition layer number increases. The solid-state transformations of the alloy were 'mapped' with the thermal history and it was found that due to the deposition of layer 'n + 1', a characteristic layer consisting of two regions heated below and above the beta transus, form in layer 'n'. The highest temperature gradients were shown to be in the first layer of deposition while the second layer is being deposited. The highest heating rate, as expected, occurs at the top of a deposition layer. For a given deposition layer number, the heating rate is greatest for the fastest laser velocity, but this effect decreases with layer number. Increasing the power for a constant traverse speed increases the peak temperature, peak width and the depth/time of melting, while also decreasing the heating rate.

5. Conduction heat transfer, modeling and diagnostics

Below and in the vicinity of the melt pool and mushy zone exists a region of substantial temperature and heat transfer relative to the environment and the remainder of the part. This 'heat affected zone' (HAZ) consists of considerable temperature gradients as a result of the laser-initiated melt pool, phase-change heat transfer and surrounding environment. Heat transfer within the HAZ is predominantly sensible (conduction) in pre-deposited layers [13]; however, latent heat transfer occurs within the mushy zone and re-melting can occur for excessively high laser powers. The depth of the HAZ may be referred to as the penetration depth which is a function of part height, power and temperature.

The repetitious passing of the laser over a solid region of the part results in 'thermal cycling' effects – characterized by localized temperature field disturbances with sharp temperature increases, instantaneously high cooling rates and then modest-to-low cooling rates. Due to thermal cycling, the average temperature of the part can increase with time depending on the thermal mass of the part and substrate, as well as the time between layer deposits (or idle time). This temperature behavior results in heat treatment, or solid state transformations, which then leads to microstructural evolution and thermomechanical interactions such as residual stress formation and thermal warping. The analytical modeling of the heat transfer inherent to DLD-processed parts has borrowed from the modeling efforts toward similar-natured welding processes. Numerical simulations of DLD are common and incorporate sensible/latent effects while also addressing the issue of mass addition.

5.1. Modeling

Based on typical laser powers and laser beam areas, heat fluxes on-the-order of 500 kW/cm^2 are easily achievable during DLD. This ultra-high heat flux is responsible for initiation and sustainment of the melt pool and HAZ, as well as the temperature gradients within them both. The mismatch in the heat source area to that of the part gives rise to a 'thermal spreading' resistance which is unavoidable and in fact dominant within the DLD process – resulting in a significant temperature rise within the melt pool that increases with power [161]. Higher heat fluxes will increase the dimension of the HAZ as well as the bulk part temperature field [33]. In order to accurately predict HAZ temperatures, analytical and numerical models can be employed. In either case many idealizations and assumptions must be integrated in order to solve the DLD/HAZ problem. The dimension of the HAZ is typically sought and minimized in order to reduce the tendency of re-processing/re-melting previously deposited layers – resulting in inadvertent microstructure evolution.

The conduction heat transfer in the solid part during DLD can be analytically modeled by utilizing solutions from arc- and laser- welding boundary value problems [103,142,143,162–169]. In many welding boundary value problems, the heat equation is solved in either cylindrical or Cartesian coordinate space for the transient, multi-dimensional temperature field. Separate from the mass addition, welding and LENS are quite similar – in that a

moving, near-point (or Gaussian) heat source is traversing along the part surface/boundary. An internal, volumetric heat generation term may also be utilized to mimic the surface heat transfer [170].

Perhaps the most referenced analytical solution for the temperature field in a part undergoing a moving heat source (with constant velocity and flux) at the boundary is that provided from Rosenthal [162]. This now-classic solution to the heat equation aids in predicting cooling rates and the HAZ penetration depth for applications such as arc-welding and friction stir welding. The semi-infinite domain solution provided by Rosenthal solves the heat equation in Cartesian space while assuming quasi-stationary conduction and neglecting nonlinear effects of temperature-dependent material properties and latent heat of transformation. The presented solutions are centered in vicinity of the HAZ with Lagrangian-type reference frames (origin follows the heat source). Results demonstrate that the HAZ temperature decreases exponentially with traverse speed. For example, the quasi-steady, two-dimensional temperature field (x–z coordinates) in the LENS-deposited thin wall structure can be approximated using the Rosenthal solutions [171], as:

$$\bar{T}(x^*, z^*) = e^{-x^*} K_o\left(\sqrt{x^{*2} + z^{*2}}\right) \tag{16}$$

where K_o is the modified Bessel function of the second kind and zero order. Spatial coordinates and lengths, including the average heat transfer coefficient, are normalized by the term: $2k/\rho cV$ and the temperature field is normalized using the term: $\alpha q/\pi kt$.

For laser and electron-beam welding/processing, the Rosenthal solution is still applicable, however, the heat source is now somewhat smaller and the HAZ penetration depth is deeper – forming 'keyholes' (cavities) which require separate attention. Different analytical approaches are warranted as the moving point heat source described by many traditional welding models is inaccurate. Swift-Hook and Gick [165] provided a theoretical foundation for penetration welding with lasers. They utilized a line heat source within a moving medium and respected the temperature-dependence of thermophysical properties. Their model demonstrated that faster beam/plate relative motion results in smaller melt pools and HAZ size. Their work demonstrated that it is not always desirable to achieve high energy transfer and melting efficiencies, but that establishing a narrow HAZ with high penetration depth per unit power should be sought [165]. Later, Steen et al. [172] proposed a model for laser welding that utilized a combined point/line heat source to better capture surface irradiation along the domain. Klemens theoretically demonstrated the effect of vapor flow in penetration cavities during electron and laser beam welding [173]. It was shown that electron and laser beams provide for different HAZ penetration depths, as the electron beam HAZ is more sensitive to collimation (parallelism of beam rays). Andrews and Atthey demonstrated that melt pools with higher surface tension can reduce the penetration depth during laser/electron-beam welding and described a hydrodynamic limit associated with steady welding processes [166]. Mazumder and Steen provided a detailed analysis of the heat transfer occurring during laser welding, especially with regard to the keyhole region and effects [167]. Their model allows for heat loss from upper/lower slab (semi-infinite) surfaces, keyhole formation and is capable of estimating metallurgical phenomena and weld penetration depth.

For the DLD process, the boundary value problem is complicated by the presence of continual mass addition via blown powder (or wire feedstock), allowing the part's volume to grow with time. This added complexity makes the generation and/or utilization of analytical solutions very difficult. Nonetheless, the analytical methods and results from arc, laser and/or electron-beam welding/processing provide a necessary starting point while their
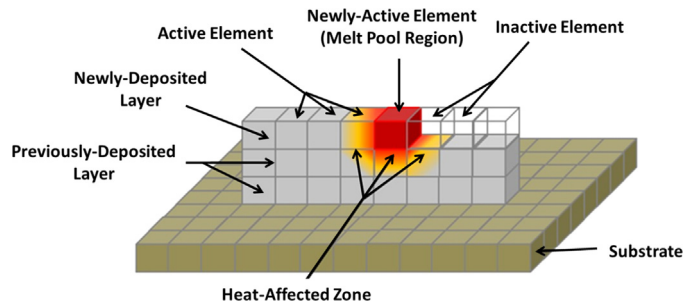

Fig. 12. Numerical modeling of a thin wall via DLD.

solutions provide valuable insights into the DLD/HAZ heat transport.

In-lieu of solving a complex set of governing, partial differential equations for the DLD problem, numerical simulation is employed, e.g. finite element methods (FEM) and/or computational fluid dynamics (CFD). The governing equations for energy, momentum and mass are discretized and solved numerically within the entire domain of the part during DLD. The finite element method may be used for numerically solving the discretized conservation equations via computational resources. The FEM discretizes the domain into thousands, or millions, of elements in which the conservation equations are applied iteratively using algebraic methods. In contrast to analytical methods, FEM allows for non-ideal boundary conditions and complex shapes. For instance, the heating and cooling profiles can be asymmetric while the processed part can have rivets or protrusions (as opposed to a semi-infinite domain). Krutz/Segerlind and Goldak et al. first utilized FE to model the moving heat source welding problem [170,174]. In these early demonstrations of FE for welding, the highly coupled conservation equations were solved and the results were shown to match analytical and experimental results with minimal error.

Numerical simulation of DLD has been performed by many authors in recent history [48,49,107,115,134,150,152,154,175, 176]. Much of this work has focused on the simulation of thin wall ('single line') builds which are more easily validated via experimental measurements and require less computational resources. The common challenges in numerically modeling the DLD process are incorporating: mass-addition, multi-track deposition effects of 3D objects, temperature-dependent properties, melting/solidification and the melt pool fluid dynamics/wetting behavior. The meshing scheme and dimensionality of the simulation is also important – as this can provide for more accurate results. Thermo-kinetic models may be utilized to couple the temperature field with empirical microstructure-property relations to aid in predicting the microstructural distribution in the part [48]. Solidification can be accounted for in various approaches, including the 'enthalpy method' [176], continuous cooling transformation (CCT) diagrams [150], cellular automation techniques [158] and inelastic deformation energy dissipation [152].

A typical approach to simulating the mass addition (or 'massification') is by solving a series of constant-geometry problems – each for a given time. For each new time, new elements are introduced to the mesh and the neighboring mesh is then connected and initial conditions are fed in while boundary conditions are updated, as shown in Fig. 12. Each new, 'activated' element (or 'birthed cell') has an initial temperature near-equal to the material liquidus temperature. The number of new elements introduced over a time interval is then a function of the powder feed rate. Note that each element consists of sub-elements in order to better model the thermal energy diffusion and local fluid mechanics.

The energy transfer throughout the part is directly coupled with its inherent microstructural evolution. As shown by Costa et al. [48],

the thermal energy problem can first be solved for a given time step, then the microstructure determined via empirical correlations, and then the next thermal time step can be undertaken. This process is then repeated while aiming to achieve acceptable solution convergence. Yin et al. demonstrated that 2D numerical simulations provide for similar results from 3D simulations for thin wall builds during DLD, but the laser-surface coupling coefficient (absorption) must be calibrated in the 2D model to provide for a similar power level in the 3D model [49]. It was also found that the 2D model is inferior to the 3D model for predicting heat flow into the substrate – which is considerably multi-dimensional. Hence, the discrepancy between 2D and 3D simulations is higher in the early deposition layers [49].

A clear advantage of numerical and/or analytical modeling is that they provide an important means to 'virtually' run experiments to determine optimal DLD process parameters. This is more cost-effective and less time-consuming relative to trial-and-error experimentation with difficult measurement techniques. Utilization of numerical methods provides a more efficient means to optimize the DLD process for producing parts with targeted post-manufactured properties. Via numerical simulation, and in-lieu of expensive/extensive experimentation, end-users can, for example, learn and provide (i) the cooling rates, (ii) thermal cycle frequency/amplitude in the HAZ and (iii) peak temperature distribution. Such 'thermal data' can then be used for coupling with microstructural evolution in the part – which can then be empirically or directly related to part thermomechanical integrity and performance.

5.2. Bulk heating and thermal cycling

Due to the temperature gradient between the melt pool and the substrate, conduction heat transfer through the part thickness occurs. In addition, due to temperature difference between the part and environment, convective/radiative heat loss occurs simultaneously – giving rise to the familiar conjugate-type, hyperbolic heat transfer found in many extended surfaces/fins. Due to the conjugate heat transfer between the melt pool and substrate, and repetitious laser passes, the part is subjected to thermal cycling during DLD. This repetitive heating/cooling of the part can result in heat treatment and microstructure evolution; hence, this conjugate-type heat transfer ultimately dictates the microstructure of the post-fabricated part and thus its mechanical properties. Costa et al. showed that repetitive deposition, occurring with multiple track deposits on AISI P20 steel results in repetitive tempering of martensite [48] while Wang and Felicelli [102] provided a correlation, which depended on the number of thermal cycles imposed on the part, to predict the proportion of retained martensite during the cooling of AISI 410 SS to ambient temperature.

Griffith et al. integrated type-C (tungsten/rhenium) thermocouples directly into a sample of H13 tool steel during LENS fabrication and the results were correlated with post-fabrication hardness [6,34]. The thermal response of the bottom-layer was recorded in real-time during DLD and the effect of laser rastering on the bottom layer temperature is shown in Fig. 13. It may be seen that additional deposition layers lead to a thermal spike throughout the part and this alleviates any microstructure typically realized during rapid quenching. Although a rapid quench occurs, the repetitive passing of the laser relaxes the microstructure in the post-deposited structure. The thermal spike for a given location along the height of the part decreases with time as the height of the part increases by the addition of more layers. Griffith et al. found that the final deposited layers, which experienced less thermal cycling and integrated heat treatment,
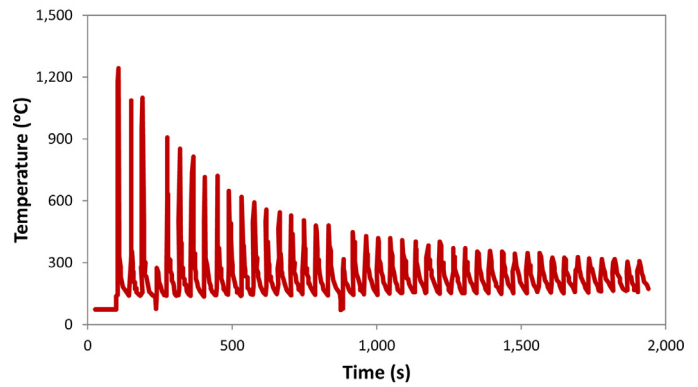

Fig. 13. Characteristic temperature response vs. time for a substrate-level thermocouple during LENS of H13 tool steel [13].

had higher hardness relative to the initially deposited layers [13].

For a DLD process with minimal-to-no idling between deposition, there is a nominal temperature hike that occurs with time in which the bulk temperature of the part heats incrementally with each new layer, as shown in Fig. 13. This 'integrated reheating effect' (integrated heat treatment) can adversely affect the residual stress and mechanical strength due to aging or tempering effects [13]. This bulk, sensible heating of the part can result in significant reduction in cooling rates and altering of the melt pool shape during the high-numbered deposition layers. A part with a higher bulk temperature and hotter HAZ, will lead to a bigger melt pool size with higher temperature [48]. Although the melt pool temperature does increase with layer number, this increase is asymptotic [33]. In addition, the superheat in the melt pool will influence the part thermal history by increasing the mean bulk temperature of the part with respect to time [50]. For a non-controlled, time-invariant traverse speed and laser power, the DLD part will start getting thicker/wider with each newly deposited layer; giving rise to a larger HAZ and the mushrooming effect [35,48,51].

In addition to the thermocouple experiments conducted by Griffith et al., Peyre et al. utilized 0.2 mm diameter, type-K thermocouples to measure the substrate's thermal history during the coaxial-DLD of a thin wall of Ti-6Al-4V [107]. The thermocouples were spot-welded to the substrate as close as possible to the first deposition layer. Peyre et al. demonstrated that the first deposited layer provides for the highest transient temperature response, with estimated heating and cooling rates on-the-order of 8000 K/s and 1500 K/s for titanium alloy, respectively [107].

Wang et al. demonstrated that the temperature gradient along the laser scan direction is less than the temperature gradient along the height of a thin-wall of stainless steel via DLD. The highest lengthwise temperature gradient was shown to occur near the solid-liquid interface [34]. The higher, height-wise temperature gradient was attributed to the heat sinking effect of the build substrate. Partial re-melting of previously deposited layers can occur during DLD, but this is based on the penetration depth of the melt pool and HAZ. Wang and Felicelli [102] demonstrated that approximately 1.5 layers are melted for each pass; however, as the traverse speed increases, the melt pool becomes more elongated and does not penetrate into previous layers. Slower traverse speeds result in longer laser/surface interaction times which then leads to reduced temperature gradients within the bulk part [177]. Crespo and Vilar attribute the main mechanism for heat transfer along the wall to conduction heat transfer from the HAZ to the substrate – and thus

lower 'height-wise' temperature gradients can result in decreased cooling rates [177].

Significant temperature gradients in the part can result in thermal deformation and the inheritance of residual stress [178]. This is due to thermal strains being developed between successive layers due to anisotropic shrinkage in deposition layers. This further leads to stress gradients resulting in part warping and distortion [178]. Patel and Patel numerically demonstrated that the height-wise thermal stress is dominant and that the starting point for each new deposition layer has a strong effect on the intensity and distribution of thermal stress [179]. Long et al. demonstrated that the thermal stress is nearly twice in magnitude at the first track deposit relative to the last track deposit – indicating that the start point of each layer has a very strong effect on the thermal stress distribution in the part [176].

5.3. Effect of substrate and idle time

The size, thermal capacitance and initial temperature of the substrate in which the part is built atop can have a significant impact on its temperature history and microstructure [48,50,66,153,158,175,177]. During DLD, the layer-dependent temperature difference between the melt pool and substrate provides for conduction heat transfer – which results in cooling of the melt pool and HAZ. Hence, the non-thermally controlled substrate behaves as a heat sink; especially during initial layer deposits where heat transfer to the substrate is substantial [66].

Costa et al. numerically demonstrated the 'heat sinking' effect of the substrate and its relation to the inter-layer idle time during DLD [175]. It was shown that larger substrates (for a given material) have a greater heat extraction capability while smaller substrates, and lower idle times, promote heat build-up in the part. Two substrate sizes were investigated while simulating the build of a single-track AISI 420 tool steel wall [48]; the larger substrate (61 mm long, 102.8 g) heated up approximately 5 °C per layer while the smaller substrate (8 mm long, 13.5 g) heated up approximately 27 °C per layer. This incremental heating was shown to affect the near-substrate deposition layers' microstructure and post-part hardness uniformity; for steels, tempered martensite with a relative lower hardness can exist [175]. Decreasing the substrate size or idle time – can help in reducing the amount of tempered martensite within steel parts [48,175]. Thinner substrates allow for higher cooling rates during the first deposition layer – and this results in a finer microstructure in the substrate vicinity [158].

The initial temperature of the substrate, if not preheated to a temperature closer to the melting temperature of the part material, can have a strong influence on microstructure in vicinity to the substrate since the thermal gradients during the first deposit layer can be significant. Preheating the substrate is often performed to reduce residual stress and risk of cracking and/or thermal distortion. In some cases, partial re-melting of the substrate is undergone to ensure uniformity between the substrate/part microstructure – especially in cladding processes [88]. Preheating the substrate can also alleviate cracking in compositionally gradient materials fabricated via LENS – as demonstrated via the manufacture of nickel aluminides in which the substrate was preheated to 500 °C [127]. Although preheating the substrate can allow for a higher-degree of control on the microstructure of the DLD-built part, it results in lower bulk cooling rates – thus limiting the achievable phase transformations and possibility for microstructural refinement [50,177].

The temperature rise in thin wall parts with each successive layer can be estimated (while neglecting heat loss) as [48]:

$$\Delta T_{\text{layer}} \cong \frac{\alpha P \Delta t_{\text{step}} n_{\text{steps}}}{c_{\text{p}} M_{\text{substrate}}} \qquad (17)$$
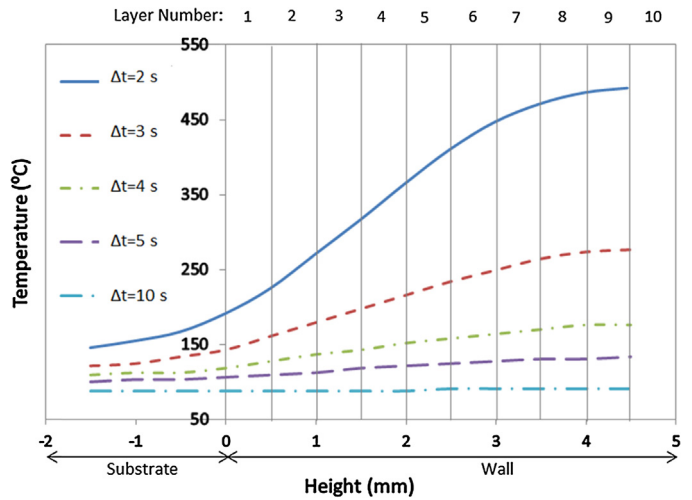

Fig. 14. Wall height centerline temperature vs. substrate thickness and deposited wall thickness for a DLD process with varying idle times, Δt, for the instant the 10th layer is started [48].

where α is the absorptivity of melt pool, P is the laser power, Δt_{step} is the idle time, n_{steps} is the number of deposition layers along a thin wall, c_{p} is the specific heat capacity of the substrate and $M_{\text{substrate}}$ is the mass of the substrate. Note that the product, $c_{\text{p}} M_{\text{substrate}}$, is the thermal capacitance of the substrate in units J/K. This equation demonstrates that larger substrates, which remain colder during the DLD process, can result in more cooling of a deposited layer. The substrate size thus has an impact on the degree of under-cooling between a newly deposited layer and the part – and this can decrease martensite formation for DLD of steels as well as the degree of re-melting of previously deposited layer.

By allowing the DLD process to cease for a user-defined amount of time, the part is allowed to cool and this reduces bulk heating effects and provides more control on microstructural homogeneity. Idling can be necessary since the deposition layer thickness with no idling (and all other process parameters held constant) can vary with respect to deposition layer number (e.g. mushrooming effect). This 'uncontrolled' deposition layer thickness increases almost linearly with volumetric exposure. The bulk temperature of the part decreases as the idle time increases and this is due to the part exchanging heat via radiation/convection in between successive layers [50]. Inter-layer idle time has a similar effect on the pre-layer deposit/wall temperature difference. As shown in Fig. 14, the isothermality of a newly deposited layer depends on the idle time – with a near-isothermal deposition layer occurring as the idle time increases [48]. Short idle times can cause re-melting of previous layers, as well as lead to warping of the part due to higher bulk temperature rises in the part with respect to time ('heat build-up') [48].

Idle time control is a simple approach for tailoring solid-state phase transformations within the bulk part. The idle time will change after each deposited layer due to the increased thermal mass of the part, but Crespo and Vilar suggest an idle time for sufficient cooling of the part to thermal equilibrium with the substrate prior to the deposition of a new layer to better ensure homogeneity in microstructure through imposition of identical thermal histories [177]. Although the idle time can be throttled for thermal control, it many cases it is sought to be minimized as to increase the speed of the manufacturing process. Layer thickness control is partially achievable via triangulation position sensors (TPSs) – laser-based devices installed in the DLD powder delivery system to control powder flow rates [27]. In addition to idle time, other layer height control methods are described in Part II.

5.4. Thermal monitoring

Monitoring of laser/welding manufacturing processes has been employed for decades [180]. With process monitoring, one is able to indirectly determine part quality based on real-time measurements within or near the manufacturing system. Monitoring allows for process automation by feeding measured data to a control loop – providing a means to better ensure part quality and process efficiency. There are several methods for monitoring laser-based processes, but it is perhaps thermal monitoring that is the most common – given the direct coupling of metallurgical bonding and heat transfer. In thermal monitoring, the outer-surface temperature field of a part is observed over a region or its entirety during processing. For DLD, this temporal temperature distribution gives vital information regarding the cooling rates, thermal gradients near the HAZ and part isothermality – which are all relatable to encumbered microstructure. The temperature and shape of the melt pool atop the part during DLD is also indicative of part/layer build integrity.

Strictly speaking, the processed part is multi-phase during DLD – with molten metal, e.g. the melt pool – near the HAZ and solid metal throughout the majority of its volume (along previously deposited layers). Hence, the temperature distribution is typically resolved to the planar temperature field of the melt pool and the profile view of the bulk part. Since the chamber within a typical DLD machine is not conducive for invasive measurement equipment, the non-invasive application of thermography and pyrometry is ideal. As shown in Fig. 2, thermography and pyrometry are accomplished with instruments such as infrared/thermal (IR) cameras and pyrometers, respectively. A thermal camera is typically used to measure the external/side temperature distribution, and thus the thermal history, of the part, while an optical pyrometer is used to observe the melt pool temperature – with a line of sight collinear to the laser. Thermal cameras can also be mounted directly to the deposition head for measuring the thermal profile of the melt pool atop the as-built part. A pyrometer may also be placed, in-lieu or in addition to a pyrometer collinear with laser, to the side of the part – pointed diagonally downwards to measure melt pool temperature [32].

Purtonen et al. [180] have provided a detailed literature review of non-contact temperature measurement methods for DLD and laser cladding. Out of twenty papers surveyed, ranging from 1994 – 2013, it is shown that the majority of equipment used for monitoring either the melt pool or part temperature characteristics are thermal cameras and pyrometers. DLD machines can come with pyrometers and/or infrared cameras installed to aid in 'closing the loop' for feedback-controlled manufacturing. One can also retrofit a DLD machine with third-party, or self-built, thermal diagnostic systems that consist of a thermal camera and/or pyrometer and data interpretation/control software [36]. This combination of thermal monitoring and control can allow for process/parameter control in real-time based on the temperature of the melt pool and/or temperature field of the part. Real-time thermal diagnostics also provides a means to perform model validation and verification.

Thermographic images are limited by the resolution, sampling rate and integration time of the imaging equipment. The maximum temperatures that occur during DLD for some materials also require high-temperature calibration or highly customized equipment. The temperature of the HAZ and melt pool will emit radiation in the infrared (for many metals); emitting more visible radiation (i.e. shorter wavelengths) as the temperature increases. Metals that appear 'red hot' are optically expressing thermal radiation in the visible wavelength range and this occurs for metals in excess of 500 °C. Since the parts during DLD will change color with increasing temperature, the wavelength-dependence of thermal radiation is observable. The emissivity of measured surfaces is typically assumed as 'gray' – indicating near wavelength-independent emission. This is assumed because most IR equipment measure radiation over a range of wavelengths [37].

The absolute temperature at a specific point is determined from the measured electromagnetic (thermal) radiation. However, this temperature can only be determined if the surface emissivity of the point-of-interest is established. This can be a challenge due to there be a significant lack in emissivity data for surfaces undergoing DLD [13,37]. The emissivity of the part during DLD-processing is non-constant and varies with space and time – due to the complex nature of the DLD process. Griffith et al. [13] proposed a method for determining the absolute temperature based on the relative temperature measurement utilizing Wien's law in conjunction with the thermal detector signal, e.g.:

$$S_i = \varepsilon c_1 \lambda_e(T)^{-5} \exp(-c_2/\lambda T) R(\lambda) \tag{18}$$

where $R(\lambda)$ is the detector response and $\lambda_e(T)$ is the temperature-dependent, effective wavelength. Then, an independently measured temperature, T_o, can be used with the temperature at the ith detector element, T, as related to the signal, S_i:

$$\frac{1}{T} = \frac{1}{T_o} + \frac{\lambda_e(T)}{c_2} \ln \frac{S_i}{S_{i,o}} \tag{19}$$

These equations can then be used, along with a proper expression for $\lambda_e(T)$, to determine absolute temperature measurements. Hammell et al. [37] demonstrated that relative temperature methods are more accurate for DLD environments with low directional radiation.

Pyrometers are suitable for thermal radiation with wavelengths in the visible and infrared spectrums, between 0.5 μm and 8 μm. Relative to thermal cameras, the field of view is much smaller; therefore, such devices are sometimes referred to as spot pyrometers – as they are only able to measure a local temperature as opposed to obtaining a temperature distribution. Pyrometers can be used in variety of high-temperature applications; with maximum temperature limits near 3300 K [181]. Pyrometry provides a means to measure the surface temperature over a wider spectral range. This is beneficial to DLD, since oxide formation along the part (melt pool) can directly impact the uniformity of its emission.

Dual-wavelength pyrometry determines temperature, independent of emissivity, by utilizing a ratio of relative radiation intensities at two different wavelengths. This method has been used to measure the melt pool temperature during DLD [31,35,36]. Dual-wavelength pyrometers are desirable as they can be utilized with no a priori knowledge of melt pool emissivity. They aid in overcoming the complexity related to estimating the emissivity of a highly transient melt pool free surface – which consists of complex oxide layers and continual powder addition at its boundary. Therefore, there is a high degree of uncertainty in the spectral properties of the melt pool surface (e.g. emissivity, absorptivity, reflectivity, transmissivity); thus, dual-wavelength pyrometry is utilized to help in eliminating the need to know such spectral properties. Methods for calibrating IR equipment based on unknown emissivity exist; however, a second, independent temperature measurement must be utilized – such as from a thermocouple or dual-wavelength pyrometer [182]. This is referred to as emittance adjustment.

Semiconductor charge-coupled devices (CCD) or active pixel sensors in complementary metal–oxide–semiconductor (CMOS) cameras can be used for investigating more moderate temperature phenomena during DLD [13], but with appropriate filtering can be used for melt pool monitoring [180]. These devices can be utilized for monitoring regions emitting wavelengths within the visible spectrum or for monitoring the HAZ of metals with low melting temperatures. Regions with visible emission include 'far-field' regions of the part where detrimental effects such as balling phenomena or change in deposition height can occur.

Contact-type temperature measurement instruments may also be utilized to thermally monitor the DLD process. At the price of spatial resolution, the integration of thermocouples (typically type-C) to the part allows for more resolution at the time-scale. Since the part is additively manufactured, it is intuitive to first integrate thermocouples along the first layer of deposition [13]. Then, with successive layers, the thermocouple will measure the thermal diffusion through the part – in correspondence to the laser scan pattern – as shown in Fig. 13. The thermal history for a given location on the part (again, most typically at the bottom) is then visualized as a time-variant thermal response indicative of the thermal cycling behavior. Although thermocouples provide valuable insight into thermal cycling, non-invasive surface temperature measurements are more often desired due to the presence of blown powder debris, elevated temperatures and molten metal. In addition, part continuity or process is not disturbed with an instrument (e.g. thermocouple).

Although thermal monitoring can aid in enhancing the DLD process efficiency, the DLD build chamber is not conducive for applied thermography. Approximately two thirds of the laser radiation is scattered/reflected and this can affect measurement equipment. Furthermore, fine powder particles partially obscure the line of sight, and the region to be measured constantly changes position. The relatively harsh environment in near-proximity to the DLD melt pool consists of many sources of thermal radiation that can affect measurement accuracy, and this includes scattering, reflection and plasma interaction [180]. The surrounding environment of the target-of-interest must also be accounted for. Objects near the target can provide for interfering radiation that reflects off the target. Surrounding blown powder and the inert gas also provide for scattering and absorption of the thermal radiation. Another final source of error is attributed to instrumental 'noise', and this can typically either be quantified or corrected.

6. Conclusions and ongoing challenges

Direct Laser Deposition (DLD), a form of Directed Energy Deposition (DED), has demonstrated to be an effective means for additively manufacturing metallic parts via simultaneous delivery of electromagnetic energy and feedstock. Although, wire and powder preforms are available, the blown-powder DLD process is generally more common since it provides for finer deposition features and is less prone to external vibrations. Blown-powder DLD has roots in successive/build-up arc welding, but matured with its commercialization as Laser Engineered Net Shaping (LENS) at the turn of the 21st century – a research product of Sandia National Laboratories. Current LENS machines offer multiple nozzles for powder deposition (as opposed to single nozzle) allowing for functional-grading and multi-material/component systems. Relative to laser-based, powder-bed fusion (PBF-L) methods, such as Selective Laser Melting (SLM), DLD allows for, in addition to functional-grading of materials, rapid repair and cladding and multi-axis deposition. The DLD technology may be relatively easier to thermally monitor and control since no powder bed obstructs previously deposited layers during manufacture. Both PBF-L and DLD are attractive additive manufacturing methods for metals since their operating chambers only need to be purged with inert gas. Powder-bed and DED methods that utilize electron beams require chambers with full vacuum conditions and this is typically more costly.

The DLD process can be physically modeled and simulated, and this aids in both technology development and in determining optimal process parameters. To this end, many transport phenomena inherent to the DLD process, and their impact on resultant microstructure, must be fully understood. Many DLD transport mechanisms have been highlighted in this Overview and it has been demonstrated that the blown powder dynamics, laser interaction, melt pool dynamics, heat affected zone (HAZ) geometry, solidification and bulk thermal cycling all play a pivotal role in establishing desired track density, morphology and microstructure.

The laser power transfer to the blown particles and melt pool is vital for achieving track/layer formation during the additive fabrication of a part. The blown powder absorbs and scatters incident, collimated electromagnetic radiation that typically consists of a Gaussian intensity profile. This scattering/absorption results in laser attenuation; with the delivered melt pool energy being, at times, significantly less than the laser power prior to intersecting the powder jets. The melt pool absorptivity will also impact the utilized laser power for layer formation; and this transient spectral property is sensitive to melt pool stability, morphology, material and oxidization. Powders have been shown to melt, evaporate and form plasma mid-flight – and this will depend primarily on the laser-to-powder heat transfer and powder size. Plasma formation during high power DLD, and higher powder feed rates, can also contribute to laser attenuation. Maximum powder efficiency is achieved when the powder jet stream diameter is matched to that of the incident laser beam.

The melt pool is the bridge between powder deposition and part. Its temperature distribution and fluidic/wetting behavior dictates solidification heat transfer and thus encumbered microstructure. Therefore, its modeling and diagnostics are of immediate interest for DLD quality control. At the boundary of the melt pool, convection and thermal radiation occurs with the chamber gas and far surroundings, respectively, and this can account for ~10% of the original, incident laser power. Heat transfer coefficients in vicinity of the melt pool are on-the-order of $10 \, W/m^2 \, K$, and as the melt pool temperature increases, both radiation/convection will increase, as well. Spatiotemporal variation in melt pool emissivity occurs due to its free surface, temperature changes and oxide formation. As the melt pool emissivity decreases, its internal temperature becomes more isothermal; however, melt pool emission has only a weak influence on its overall shape and area. The particle catching ability of the melt pool (i.e. powder efficiency) typically increases with deposition layer due to bulk heating effects in the part.

The temperature gradient across the melt pool can be significant and on-the-order of 100–1000 K/mm, while peak temperatures can be 40% higher than the material liquidus indicating a substantial level of superheat. A near-Gaussian temperature profile exists along the radius of the melt pool, with more linear behavior existing along the trailing edge where temperature gradients are smaller. The melt pool temperature distribution becomes more isothermal with reduced peak temperatures as the incident specific energy, which is basically the flux-to-scan-speed quotient, decreases. Although the temperature distribution in the melt pool is indicative of thermal/fluid transport, it has been demonstrated that controlling the DLD process for a constant melt pool temperature does not necessarily result in uniform track morphologies. Excess superheat in the melt pool can lead to vapor recoil (boiling), thus affecting solidification heat transfer and melt pool stability.

For constant (uncontrolled) laser power and minimal layer-to-layer idling, parts constructed via DLD can experience bulk heating effects, in which the average part temperature increases steadily with layer number. In addition to idle time, this heat accumulation depends on the heat transfer with surroundings, build plate thermal capacity and overall size of the part. Heat accumulation can be detrimental, as the melt pool wetting behavior, temperature and morphology can evolve – thus giving rise to a mushrooming-effect which describes wider-than-intended deposit tracks. To combat the bulk temperature rise, one can increase the layer-to-layer idle time or impose thermal control via surrounding/substrate or time-variant laser power. The specific energy incident on the melt pool plays an important role in melt pool dynamics and deposited

track morphology. In general, as the specific energy increases, the deposited-layer width, depth and height increase; however this trend is non-linear and a global maximum can exist. Melt pool shape is highly sensitive to scan speeds, typically elongating and becoming shallower at faster scan speeds. It has been demonstrated that the aerial topology of the melt pool is not a strong indicator of its overall morphology (e.g. via pyrometry), as the depth-to-aerial-area ratio is non-unique. Level set theory can be used to model the melt pool morphology.

Surface-tension-driven flow along the periphery of the melt pool, or Marangoni convection, depends strongly on the temperature sensitivity of the liquid-to-solid surface tension of the metal utilized. This temperature sensitivity, which can also be expressed in terms of the Marangoni number, can be negative or positive; with negative Marangoni numbers representing melt pools with a wide/shallow form factor and center-to-edge directional flow and positive Marangoni numbers describing a narrow/shallow melt pool with edge-to-center directional flow. Marangoni convection flows typically have higher peak velocities than free-convection type flows (density variation driven) and this can result in increased laser energy utility. Melt pools with small surface temperature gradients are more prone to evaporation and this can decrease their peak temperatures. Positive Marangoni numbers describe a melt pool that generates fine microstructures concentrated near its bottom, while negative Marangoni numbers describe deposited tracks with finer microstructures near the top. Melt pools inherent to DLD can also consist of flows driven by thermocapillary and disjoining pressure differences. In addition to free-convection and Marangoni-type flow, these flows will govern solidified track morphologies. It has been shown that the flow in the melt pool can be turbulent with speeds on-the-order of 1 m/s.

Solidification heat transfer between the melt pool and previously deposited tracks dictates the encumbered microstructure in DLD parts. Marangoni convection can aid in mixing the melt pool for alleviating macro-segregation effects, and metals with higher surface tension will have higher melting rates along the melt pool centerline. It has also been shown that melting efficiency can increase with higher laser powers and traverse speeds. Solidification heat transfer must be controlled as it can lead to porosity in manufactured parts due to lack of fusion, and this is more likely to occur at the beginning of a relatively colder layer deposit; especially near the substrate. The cooling rate of the melt pool will dictate the microstructures formed in a deposited layer; with higher cooling rates resulting in finer microstructures. For DLD, the cooling rate increases with higher scan speeds and can be on-the-order of 10,000 °C/s. The initial cooling rate for a layer can decrease with layer number due to bulk heating effects. The quotient involving the melt pool thermal gradient and solidification velocity has a strong influence on encumbered microstructure phase.

The heat affected zone (HAZ) is the region directly below and surrounding the melt pool and consists of strong temperature gradients and elevated temperatures. The dimension of the HAZ is strongly dependent on laser flux, which can be as high as 500 kW/cm^2, and influences the degree of re-melting in previous layers. Reduced laser focus areas will result in higher heat fluxes and this can lead to hotter melt pools and vapor recoil. Thermal cycling occurs along solidified layers due to multiple passes of the laser for successive layer deposition, and this can result in microstructural evolution. The impact of thermal cycling will depend on the thermal mass of the part being fabricated and the layer-to-layer idle time. The heat transfer from the melt pool to the substrate is reminiscent of the conjugate heat transfer found in many extended heat transfer surfaces (i.e. fins). Residual stress formation can occur due to high thermal gradients between adjacent layers and this can lead to part warping; hence, temperature control of the HAZ and melt pool is paramount for ensuring final part quality. At the price of

cooling rates, the temperature, size and thermal capacitance of the substrate can be controlled to govern the conjugate heat transfer and thus the degree of thermal cycling and bulk heating.

Analytical and numerical modeling of the blown-powder DLD process borrows from the fundamental concepts of arc/laser welding; however, the boundary value problem is severely complicated by the instability of the melt pool free surface due to powder addition. Finite element methods (FEM) and computational fluid dynamics (CFD) are commonly employed to model the multi-physical DLD problem. To date, the majority of simulations have focused on two-dimensional bodies with a single-deposit width (i.e. thin walls) as the meshing scheme needs to be highly resolved and dynamic – to accurately model the high heat flux transport and deposition. Solidification heat transfer is typically modeled using continuous cooling transformation diagrams, cellular automation techniques and inelastic deformation energy dissipation.

Non-destructive evaluation (NDE) of the DLD process has been accomplished via the use of substrate-level thermocouples and/or thermal cameras that monitor the temperature of the melt pool and bulk part. Dual-wavelength pyrometers are typically employed to monitor melt pool temperature while infrared cameras are utilized to monitor bulk temperature response in the part (i.e. near the HAZ). The utilization of NDE allows for closed-loop feedback control on laser power and thus provides for the unique opportunity to combat effects such as bulk heating and for controlling melt pool dynamics. Thermographic images are valuable for characterizing the thermal/fluid phenomena inherent to DLD and aid in determining "target" temperature histories for desired microstructures.

Significant progress has been made in many facets of DLD in the past two-to-three decades. Advancements in DLD technology, characterization and modeling are now driving the next-generation of DLD machines and processing. However, as the field of LBAM moves forward, the utilization of DLD for fabricating functional metallic parts will greatly depend on overcoming many significant challenges. The future, widespread utilization of DLD, and its commercialization, is at stake. Competing technologies such as PBF-L are becoming more affordable and available to industry and academia. Although DLD will remain a means to accomplish LBAM – especially for repair/cladding and the manufacture of functionally graded and/or customized materials, its widespread application and evolution will depend on championing many current obstacles.

Some of the major challenges facing DLD are summarized below and are in no particular order of difficulty or importance.

(1) *DLD efficiency*: The DLD process is not highly efficient. There is significant waste of energy and blown powder during the process. Although wasted powder can be reclaimed for later use, the deposition and energy efficiencies should increase to make the DLD process less costly. Further, the DLD laser-to-melt pool heat transfer is inefficient due to optical limitations (laser attenuation) and heat loss to surroundings. It is worth investigating more appropriate energy/deposition methods as to increase overall efficiency.

(2) *DLD control*: Time-invariant operating parameters, descriptive of an un-controlled DLD process, will result in anisotropic parts and/or parts that fail during the build. The future of DLD is clearly headed toward real-time DLD control – allowing for adaptive, time-variant operating parameters based on feedback from on-site monitoring. However, application of monitoring/control hardware and software in DLD machines is still not widespread – especially in comparison to traditional laser-based manufacturing processes [183]. Nonetheless, monitoring of DLD processes is currently more mature relative to PBD-L processes (e.g. SLM) – since the powder bed can cover the previously deposited surface temperatures. In order to achieve more widespread implementation

of monitoring/control hardware in DLD machines, the packaging of a laser-adaptive DLD machine is needed. A simple approach to controlling the thermal history during DLD is through process idling between layers; however, more novel ways for achieving control can be through "active substrates" in which extracted heat can be managed and/or via chamber-controlled heat transfer. By achieving a degree of control over the DLD process, end-users can manage the encumbered microstructures, and their resultant homogeneity, in real-time.

(3) *Numerical modeling:* Current limitations in computational software and hardware are making it difficult to model all of the inherent DLD phenomena accurately and with high-fidelity. Next-generation of DLD simulative models should allow for time-variant process parameters and the accurate modeling of blown powder dynamics, melt pool morphology and melt pool fluid dynamics/wetting behavior. In addition, multitrack DLD simulation and the modeling of more realistic/complex shapes must be undergone using either supercomputing resources or creative modeling approaches. To model the DLD process, state-of-the-art in solidification simulation must be employed and this may require the use of empirical data; however, an agnostic solidification model that is independent of material would be ideal.

(4) *Determination of process parameters:* Achieving near net-shaped and fully dense parts requires knowledge of the optimal process parameters for a given DLD machine. Ideally, these parameters should be known prior to building parts. However, it is typical to have to first determine the parameters based on trial-and-error. Although parameters are reported in the literature, they can only be used as a starting point since DLD machines vary in design. For example, one DLD machine can have a single nozzle, while a LENS machine can have multiple nozzles. Round-robin learning for optimal DLD process parameters for various materials needs to be substituted with dynamic/adaptive learning procedures combined with numerical simulation. A materials and procedure "genome" must be initiated and built-upon as to accelerate DLD-machine/procedure learning.

(5) *Industry adoption:* The adaptability of DLD to industry will require flexible process speeds and maximal substrate utilization. The challenge is going from 'the lab to fab' and providing a DLD process with high certainty and repeatability with features novel for either low or high volume production. Further, in order to use DLD (or any AM process for that matter), trained technicians are required for initial setup and process monitoring. A future workforce must be trained and perhaps certified. For maximal substrate utilization, more research needs to be conducted to determine how DLD process parameters should change as the number of parts/plate, or the size of the part, increases [184].

(6) *Radiative properties:* The laser attenuation and part emission/irradiation all depend on highly complex radiative properties of the laser, blown powder, melt pool and part. There is significant uncertainty in these properties and they must be better characterized in order to better refine modeling efforts and to aid the thermal detection efforts during DLD. Further, there exists uncertainty in the incident laser power transfer to particles/melt pool due to laser attenuation and powder cloud scattering effects. Fundamental experimentation is required to quantify the spectral behavior of fluidic and/or solid bodies in a DLD-like atmosphere and operating environment.

(7) *Process monitoring limitations*: Current thermal monitoring equipment, such as infrared cameras and pyrometers, are limited to certain resolutions and sampling rates – and this can affect the accuracy and responsiveness of measurement/control. Further, the DLD environment is relatively harsh and not ideal for thermal monitoring. Thermal radiation 'noise' from surrounding bodies/gases in the DLD chamber may interfere with the accuracy of the measurements. For complex geometries, layer deposition height is non-uniform along the track and this can cause cameras to lose focus and thus generate more uncertainty in measurement [35]. Current DLD monitoring methods are optical in nature. Although acoustic methods may be used, the acoustical emissions are prone to disturbances and thus make the recorded data unreliable [180]. In this case, structure-based acoustic emissions are more reliable and could perhaps be used for crack initiation and growth monitoring. The field of non-destructive evaluation of LBAM processes is growing and novel, responsive approaches need to be developed. The next-generation of monitoring and control systems will most likely include a combination of detectors within and near the DLD chamber.

(8) *DLD of functionally graded materials*: Generation of exotic, functionally graded materials via DLD is still an active research topic. However, more work is required to fully understand how to optimize the DLD process for functionally graded material manufacture. The real-time control of multi-material powder delivery is difficult; however, parameters for each new layer can be set while the machine idles. Thermal monitoring of multi-material DLD parts will require truly novel approaches since the emittance of each material will vary. Process parameter optimization for functional-grading via DLD will depend on the concentration gradients of each material and may require significant trial-and-error. The single-material/process genome for DLD should have "rules" for extending to multi-material systems.

(9) *Near net shape:* The DLD process typically generates parts with a positive net shape; meaning, a post-DLD process is required to bring the part to final tolerances. One of the primary challenges of DLD is to achieve perfect net shape during manufacture without any need for a secondary machining process. However, new hybrid additive/subtractive LBAM machines are emerging that consist of multiple tool/deposition heads and can perform post-AM net-shaping within the build chamber [185–188].

(10) *Standards and regulations:* As DLD evolves, there will be a need to generate and employ standards and regulations to ensure public safety and compliance. Professional societies such as ASTM International, whom have a history of generating standards for metallic parts made via traditional-manufacturing methods, has already begun the task for AM-part certification [1,189]. However, due to the anisotropy of DLD parts, the certification will need to consider post-AM processing such as surface finishing and heat treatments. The certifications will also need to consider the DLD process parameters utilized and whether any defects, such as voids/cavities, exist in the generated sample. In this sense, the DLD process may have to be certified in order to ensure quality products are being produced for post-AM mechanical certification. Once standards are in place for the DLD process and for mechanically characterizing the parts in which it produces, the more widespread application of such parts for engineering service is imminent.

(11) *Miniaturization:* Although it appears the DLD process is limited to the dimension of the preform, it will be worth investigating its use for fabricating micro-scaled products. The size of utilized preforms may need to be reduced; for example, the powder diameter can be made smaller, but this will pose new challenges in powder delivery and manufacture. The use of new substrates or external body forces may need to be utilized.

(12) *Reflective metal fabrication:* Determining a means to fabricate highly reflective materials via DLD will broaden the possible applications in which DLD is employed. For example, the DLD of copper or aluminum would allow for the rapid fabrication of heat transfer equipment. Unconventional processing approaches, including the use of new lasers, may need to be employed for fabricating such metals.

Challenges (1)–(12) hinder the widespread adoption and continual use of DLD technology. However, it is clear that significant research is being conducted on an international scale to address these issues. Overcoming these challenges will help in establishing novel relationships between part thermal history and post-DLD part performance. To this end, the microstructural features, mechanical behavior and the related DLD process optimization/control for enhanced mechanical properties are presented in Part II of this two-part Overview.

Acknowledgments

References

[1] ASTM-International, ASTM Standard F2792-12a: Standard Terminology for Additive Manufacturing Technologies, 2012.
[2] C.L. Weber, V. Pena, M.K. Micali, E. Yglesias, S.A. Rood, J.A. Scott, et al., The Role of the National Science Foundation in the Origin and Evolution of Additive Manufacturing in the United States, 2013.
[3] L. Robinson, J. Scott, Layers of complexity: making the promises possible for additive manufacturing of metals, JOM 66 (2014) 2194–2207, http://dx.doi.org/10.1007/s11837-014-1166-x
[4] Y. Tadjdeh, Navy Beefs Up 3D Printing Efforts with New "Print the Fleet" Program, Natl Def, 2014, pp. 24–26.
[5] M. Foust, D. Thomsen, R. Stickles, C. Cooper, W. Dodds, Development of the GE Aviation Low Emissions TAPS Combustor for Next Generation Aircraft Engines, AIAA-2012-0936, Nashville, USA, 2012.
[6] R. Stott, Chinese Company Showcases Ten 3D-Printed Houses, ArchDaily, 2014, http://www.archdaily.com/?p=543518
[7] K. Dalgarno, T. Stewart, Production tooling for polymer moulding using the RapidSteel process, Rapid Prototyp. J. 7 (2001) 173–179.
[8] L.-E. Rännar, A. Glad, C.-G. Gustafson, Efficient cooling with tool inserts manufactured by electron beam melting, Rapid Prototyp. J. 13 (2007) 128–135.
[9] L.E. Murr, S.M. Gaytan, F. Medina, H. Lopez, E. Martinez, B.I. Machado, et al., Next-generation biomedical implants using additive manufacturing of complex, cellular and functional mesh arrays, Philos. Trans. R. Soc. A Math. Phys. Eng. Sci. 368 (2010) 1999–2032.
[10] D.D. Gu, W. Meiners, K. Wissenbach, R. Poprawe, Laser additive manufacturing of metallic components: materials, Processes Mech. Int. Mater. Rev. 57 (2012) 133–164, http://dx.doi.org/10.1179/1743280411Y.0000000014
[11] I. Gibson, D.W. Rosen, B. Stucker, Additive Manufacturing Technologies: Rapid Prototyping to Direct Digital Manufacturing, Springer, New York, 2010, http://dx.doi.org/10.1004/978-1-4419-1120-9
[12] K.V. Wong, A. Hernandez, A review of additive manufacturing, ISRN Mech. Eng. 2012 (2012) 1–10, http://dx.doi.org/10.5402/2012/208760
[13] M.L. Griffith, M.E. Schlienger, L.D. Harwell, M.S. Oliver, M.D. Baldwin, M.T. Ensz, et al., Thermal behavior in the LENS process, in: Proc. 9th Solid Free. Fabr. Symp., Austin, USA, 1998, pp. 89–96.
[14] A.J. Pinkerton, W. Wang, L. Li, Component repair using laser direct metal deposition, Proc. Inst. Mech. Eng. B J. Eng. Manuf. 222 (2008) 827–836, http://dx.doi.org/10.1243/09544054JEM1008
[15] P.S. Korinko, T.M. Adams, S.H. Malene, D. Gill, J. Smugeresky, Laser engineered net shaping for repair and hydrogen compatibility, Weld. J. 90 (2011) 171s–181s.
[16] V. Fallah, S.F. Corbin, A. Khajepour, Process optimization of Ti–Nb alloy coatings on a Ti–6Al–4V plate using a fiber laser and blended elemental powders, J. Mater. Process. Technol. 210 (2010) 2081–2087, http://dx.doi.org/10.1016/j.jmatprotec.2010.07.030
[17] W.U.H. Syed, A.J. Pinkerton, L. Li, Combining wire and coaxial powder feeding in laser direct metal deposition for rapid prototyping, Appl. Surf. Sci. 252 (2006) 4803–4808, http://dx.doi.org/10.1016/j.apsusc.2005.08.118
[18] F. Wang, J. Mei, X. Wu, Compositionally graded Ti_6Al_4V + TiC made by direct laser fabrication using powder and wire, Mater. Des. 28 (2007) 2040–2046.
[19] A. Kratky, Production of Hard Metal Alloys, 1937, Patent # US2076952.
[20] I. Harter, Method of Forming Structures Wholly of Fusion Deposited Weld Metal, 1942, Patent # US2299747A.
[21] H.N. Farmer, Process of Rebuilding Steel Structures, 1970, Patent # US3549410A.
[22] U. Akira, Method of Constructing Substantially Circular Cross-Section Vessel by Welding, 1972, Patent # US3665143A.
[23] H.T. Brandi, H. Luckow, Method of Making Large Structural One-Piece Parts of Metal, Particularly One-Piece Shafts, 1976, Patent # US3985995A.
[24] R.F. Housholder, Molding Process, 1981, Patent # US4247508A.
[25] C.O. Brown, E.M. Breinan, B.H. Kear, Method for Fabricating Articles by Sequential Layer Deposition, 1982, Patent # US4323756A.
[26] G.K. Lewis, R.B. Nemec, J.O. Milewski, D.J. Thoma, D. Cremers, M.R. Barbe, Directed Light Fabrication, in: No. LA-UR–94-2845; CONF-9410189–2, Los Alamos Natl Lab, Los Alamos, NM, USA, 1994.
[27] F.P. Jeantette, D.M. Keicher, J.A. Romero, L.P. Schanwald, Method and System for Producing Complex-Shape Objects, 2000, Patent #: US006046426A.
[28] W. Meiners, K. Wissenbach, A. Gasser, Shaped Body Especially Prototype or Replacement Part Production, 1998, Patent # DE19649865C1.
[29] W. Meiners, K. Wissenbach, A. Gasser, Selective Laser Sintering at Melting Temperature, 2001, Patent # US6215093B1.
[30] C.R. Deckard, Method and Apparatus for Producing Parts by Selective Sintering, 1989, Patent # US4863538A.
[31] D. Salehi, M. Brandt, Melt pool temperature control using LabVIEW in Nd:YAG laser blown powder cladding process, Int. J. Adv. Manuf. Technol. 29 (2005) 273–278, http://dx.doi.org/10.1007/s00170-005-2514-3
[32] R. Ye, J.E. Smugeresky, B. Zheng, Y. Zhou, E.J. Lavernia, Numerical modeling of the thermal behavior during the LENS process, Mater. Sci. Eng. A 428 (2006) 47–53, http://dx.doi.org/10.1016/j.msea.2006.04.079
[33] T. Hua, C. Jing, L. Xin, Z. Fengying, H. Weidong, Research on molten pool temperature in the process of laser rapid forming, J. Mater. Process. Technol. 198 (2008) 454–462, http://dx.doi.org/10.1016/j.jmatprotec.2007.06.090
[34] L. Wang, S.D. Felicelli, J.E. Craig, Experimental and numerical study of the LENS rapid fabrication process, J. Manuf. Sci. Eng. 131 (2009) 041019, http://dx.doi.org/10.1115/1.3173952
[35] L. Tang, R.G. Landers, Melt pool temperature control for laser metal deposition processes—Part I: Online temperature control, ASME J. Manuf. Sci. Eng. 132 (2010) 011010, http://dx.doi.org/10.1115/1.4000882
[36] J.E. Craig, T. Wakeman, R. Grylls, J. Bullen, On-line imaging pyrometer for laser deposition processing, in: TMS 2011 Annu. Meet. Exhib., San Diego, USA, 2011.
[37] J.J. Hammell, C.J. Ludvigson, M.A. Langerman, J.W. Sears, Thermal imaging of laser powder deposition for process diagnostics, in: ASME 2011 Int. Mech. Eng. Congr. Expo., Denver, USA, 2011, pp. 41–48.
[38] A. Raghavan, H.L. Wei, T.A. Palmer, T. DebRoy, Heat transfer and fluid flow in additive manufacturing, J. Laser Appl. 25 (2013) 052006, http://dx.doi.org/10.2351/1.4817788
[39] M. Griffith, M. Schlienger, L. Harwell, Thermal behavior in the LENS process, in: No SAND–98-1850C; CONF-980826, Sandia Natl Labs, Albuquerque, NM, USA, 1998.
[40] M. Griffith, M. Schlienger, L. Harwell, M. Oliver, M. Baldwin, M. Ensz, et al., Understanding thermal behavior in the LENS process, Mater. Des. 20 (1999) 107–113.
[41] T.A. Davis, The Effect of Process Parameters on Laser Deposited Ti–6Al–4V, University of Louisville, 2004.
[42] G. Pi, A. Zhang, G. Zhu, D. Li, B. Lu, Research on the forming process of three-dimensional metal parts fabricated by laser direct metal forming, Int. J. Adv. Manuf. Technol. 57 (2011) 841–847, http://dx.doi.org/10.1007/s00170-011-3404-5
[43] L. Han, K. Phatak, F. Liou, Modeling of laser cladding with powder injection, Metall. Mater. Trans. B 35 (2004) 1139–1150.
[44] F. Vásquez, J.A. Ramos-Grez, M. Walczak, Multiphysics simulation of laser–material interaction during laser powder depositon, Int. J. Adv. Manuf. Technol. 59 (2011) 1037–1045, http://dx.doi.org/10.1007/s00170-011-3571-4
[45] L. Bian, S.M. Thompson, N. Shamsaei, Mechanical properties and microstructural features of direct laser deposited Ti–6Al–4V, JOM 67 (2015) 629–638, http://dx.doi.org/10.1007/s11837-015-1308-9
[46] Y. Xiong, W.H. Hofmeister, Z. Cheng, J.E. Smugeresky, E.J. Lavernia, J.M. Schoenung, In situ thermal imaging and three-dimensional finite element modeling of tungsten carbide-cobalt during laser deposition, Acta Mater. 57 (2009) 5419–5429, http://dx.doi.org/10.1016/j.actamat.2009.07.038
[47] J.R. Davis, Powder Metallurgy Processing of Nickel Alloys. Nickel, Cobalt, Their Alloys, ASM International, 2000, pp. 215.
[48] L. Costa, R. Vilar, T. Reti, A.M. Deus, Rapid tooling by laser powder deposition: process simulation using finite element analysis, Acta Mater. 53 (2005) 3987–3999, http://dx.doi.org/10.1016/j.actamat.2005.05.003
[49] H. Yin, L. Wang, S.D. Felicelli, Comparison of two-dimensional and three-dimensional thermal models of the LENS® process, ASME J. Heat Transfer 130 (2008) 102101, http://dx.doi.org/10.1115/1.2953236
[50] B. Zheng, Y. Zhou, J.E. Smugeresky, J.M. Schoenung, E.J. Lavernia, Thermal behavior and microstructural evolution during laser deposition with laser-engineered net shaping: part I. Numerical calculations, Metall. Mater. Trans. A 39 (2008) 2228–2236, http://dx.doi.org/10.1007/s11661-008-9557-7
[51] V.D. Manvatkar, A.A. Gokhale, G. Jagan Reddy, A. Venkataramana, A. De, Estimation of melt pool dimensions, thermal cycle, and hardness distribution in the laser-engineered net shaping process of austenitic stainless steel, Metall. Mater. Trans. A 42 (2011) 4080–4087, http://dx.doi.org/10.1007/s11661-011-0787-8

[52] P.P. Mehta, R.R. Otten, E.B. Cooper, Method and Apparatus for Repairing Metal in an Article, 1988, Patent # US4743733A.

[53] W. Konig, T. Celiker, H.-J. Herfurth, Approaches to prototyping of metallic parts, in: 2nd Eur. Conf. Rapid Prototyp. Manuf., Nottingham, UK, 1993, pp. 303–316.

[54] F. Klocke, H. Wirtz, W. Meiners, Direct manufacturing of metal prototypes and prototype tools, in: Proc. 7th Solid Free. Fabr. Symp., Austin, USA, 1996, pp. 141–148.

[55] A.W. Hammeke, Laser Spray Nozzle and Method, 1988, Patent # US4724299A.

[56] A. Buongiorno, Laser/Powdered Metal Cladding Nozzle, 1995, Patent # US5477026A.

[57] G.A. Whitlow, G.J. Bruck, J.E. Smith, Method of Producing Articles from Powder Metal, 1990, Patent # US4927992A.

[58] G.K. Lewis, J.O. Milewski, D.A. Cremers, R.B. Nemec, M.R. Barbe, Laser Production of Articles from Powders, 1998, Patent # US5837960A.

[59] R. Mah, Directed light fabrication, Adv. Mater. Processes 151 (1997) 31–33.

[60] D.J. Thoma, G.K. Lewis, J.O. Mtlewski, K.C. Chen, R.B. Nemec, Rapid Fabrication of Materials using Directed Light Fabrication, in: LA-UR–97-1385; CONF-9707101, Los Alamos Natl Lab, Los Alamos, NM, USA, 1997.

[61] G.K. Lewis, E. Schlienger, Practical considerations and capabilities for laser assisted direct metal deposition, Mater. Des. 21 (2000) 417–423.

[62] J.O. Milewski, D.J. Thoma, J.C. Fonseca, G.K. Lewis, Development of a near net shape processing method for rhenium using directed light fabrication, Mater. Manuf. Processes 13 (1998) 719–730.

[63] J.O. Milewski, G.K. Lewis, D.J. Thoma, G.I. Keel, R.B. Nemec, R.A. Reinert, Directed light fabrication of a solid metal hemisphere using 5-axis powder deposition, J. Mater. Process. Technol. 75 (1998) 165–172, http://dx.doi.org/10.1016/S0924-0136(97)00321-X

[64] D.M. Keicher, W.D. Miller, LENS moves beyond RP to direct fabrication, Met. Powder Rep. 53 (1998) 26–28.

[65] M.L. Griffith, W.H. Hofmeister, G.A. Knorovsky, D.O. MacCallum, M.E. Schlienger, J.E. Smugeresky, Direct Laser Additive Fabrication System with Image Feedback Control, 2002, Patent # US6459951B1.

[66] M.L. Griffith, D.M. Keicher, C.L. Atwood, J.A. Romero, J.E. Smugeresky, L.D. Harwell, et al., Free form fabrication of metallic components using laser engineered net shaping (LENS™), in: Proc. 7th Solid Free. Fabr. Symp., Austin, USA, 1996, pp. 125–132.

[67] C. Selcuk, Laser metal deposition for powder metallurgy parts, Powder Metall. 54 (2011) 94–99, http://dx.doi.org/10.1179/174329011X12977874589924

[68] L. Costa, R. Vilar, Laser powder deposition, Rapid Prototyp. J. 15 (2009) 264–279, http://dx.doi.org/10.1108/13552540910979785

[69] J. Mazumder, H. Qi, Fabrication of 3-D components by laser aided direct metal deposition, in: Proc. SPIE – Int. Soc. Opt. Eng., 2005, pp. 38–59.

[70] V.M. Weerasinghe, W.M. Steen, Laser cladding with blown powder, Met. Construct. 19 (1987) 581–585.

[71] J.W. Sears, Solid freeform fabrication technologies: rapid prototyping – rapid manufacturing, Int. J. Powder Metall. 37 (2001) 29–30.

[72] J. Mazumder, A. Schifferer, J. Choi, Direct materials deposition: designed macro and microstructure, Mater. Res. Innovations 3 (1998) 118–131.

[73] F.G. Arcella, F.H. Froes, Producing titanium aerospace components from powder using laser forming, JOM 52 (2000) 28–30.

[74] L. Xue, M. Islam, Free-form laser consolidation for producing functional metallic components, Laser Inst. Am. Laser Mater. Process. 84 (1998).

[75] L. Xue, M. Islam, Free-form laser consolidation for producing metallurgically sound and functional components, J. Laser Appl. 12 (2000) 160–165, http://dx.doi.org/10.2351/1.521927

[76] J. Choi, Y. Chang, Characteristics of laser aided direct metal/material deposition process for tool steel, Int. J. Mach. Tools Manuf. 45 (2005) 597–607, http://dx.doi.org/10.1016/j.ijmachtools.2004.08.014

[77] S. Ghosh, J. Choi, Three-dimensional transient finite element analysis for residual stresses in the laser aided direct metal/material deposition process, J. Laser Appl. 17 (2005) 144–158.

[78] J. Choi, Process and Properties Control in Laser Aided Direct Metal/Materials Deposition Process. Manufacturing, vol. 2002, ASME, 2002, pp. 81–89, http://dx.doi.org/10.1115/IMECE2002-33568

[79] R. Dwivedi, R. Kovacevic, An expert system for generation of machine inputs for laser-based multi-directional metal deposition, Int. J. Mach. Tools Manuf. 46 (2006) 1811–1822.

[80] R. Dwivedi, R. Kovacevic, Process planning for multi-directional laser-based direct metal deposition, Proc. Inst. Mech. Eng. C J. Mech. Eng. Sci. 219 (2005) 695–707, http://dx.doi.org/10.1243/095440605X31535

[81] F.-J. Kahlen, A. Kar, Tensile strengths for laser-fabricated parts and similarity parameters for rapid manufacturing, J. Manuf. Sci. Eng. 123 (2001) 38, http://dx.doi.org/10.1115/1.1286472

[82] F. Liou, K. Slattery, M. Kinsella, Applications of a hybrid manufacturing process for fabrication of metallic structures, Rapid Prototyp. J. 13 (2007) 236–244.

[83] J. Zhang, F. Liou, Adaptive slicing for a five-axis laser aided manufacturing process, in: Proc 2001 ASME Des Autom Conf, 2001.

[84] J. Zhang, Adaptive slicing for a multi-axis laser aided manufacturing process, J. Mech. Des. 126 (2004) 254, http://dx.doi.org/10.1115/1.1649966

[85] Y. Li, H. Yang, X. Lin, W. Huang, J. Li, Y. Zhou, The influences of processing parameters on forming characterizations during laser rapid forming, Mater. Sci. Eng. A 360 (2003) 18–25, http://dx.doi.org/10.1016/S0921-5093(03)00435-0

[86] G. Wu, N.A. Langrana, R. Sadanji, S. Danforth, Solid freeform fabrication of metal components using fused deposition of metals, Mater. Des. 23 (2002) 97–105, http://dx.doi.org/10.1016/S0261-3069(01)00079-6

[87] M. Gremaud, J.D. Wagniere, A. Zryd, W. Kurz, Laser metal forming: process fundamentals, Surf. Eng. 12 (1996) 251–259.

[88] M. Gaumann, C. Bezencon, P. Canalis, W. Kurz, Single-crystal laser deposition of superalloys: processing – microstructure maps, Acta Mater. 49 (2001) 1051–1062.

[89] K. Zhang, W. Liu, X. Shang, Research on the processing experiments of laser metal deposition shaping, Opt. Laser Technol. 39 (2007) 549–557, http://dx.doi.org/10.1016/j.optlastec.2005.10.009

[90] A. Birnbaum, P. Aggarangsi, J. Beuth, Process scaling and transient melt pool size control in laser-based additive manufacturing processes, in: Proc. 14th Solid Free. Fabr. Symp., Austin, USA, 2003, pp. 328–339.

[91] L.D. Harwell, M.L. Griffith, D.L. Greene, G.A. Pressly, Energetic Additive Manufacturing Process with Feed Wire, 2000, Patent # US6143378A.

[92] A. Heralic, A.-K. Christiansson, B. Lennartson, Height control of laser metal-wire deposition based on iterative learning control and 3D scanning, Opt. Lasers Eng. 50 (2012) 1230–1241.

[93] K.P. Karunakaran, A. Bernard, S. Suryakumar, L. Dembinski, G. Taillandier, Rapid manufacturing of metallic objects, Rapid Prototyp. J. 18 (2012) 264–280, http://dx.doi.org/10.1108/13552541211231644

[94] D. Cormier, O. Harrysson, H. West, Characterization of H13 steel produced via electron beam melting, Rapid Prototyp. J. 10 (2004) 35–41.

[95] O.L. Harrysson, O. Cansizoglu, D.J. Marcellin-Little, D.R. Cormier, H.A.I. West, Direct metal fabrication of titanium implants with tailored materials and mechanical properties using electron beam melting technology, Mater. Sci. Eng. C 28 (2008) 366–373.

[96] H. Zhang, J. Xu, G. Wang, Fundamental study on plasma deposition manufacturing, Surf. Coat. Technol. 171 (2002) 112–118.

[97] W. Hofmeister, M. Wert, J. Smugeresky, J.A. Philliber, M. Griffith, Investigating solidification with the laser-engineered net shaping (LENS) process, JOM 51 (1999) 6–11.

[98] M. Grujicic, G. Cao, R.S. Figliola, Computer simulations of the evolution of solidification microstructure in the LENS rapid fabrication process, Appl. Surf. Sci. 183 (2001) 43–57, http://dx.doi.org/10.1016/S0169-4332(01)00553-0

[99] Z.L. Lu, D.C. Li, B.H. Lu, A.F. Zhang, G.X. Zhu, G. Pi, The prediction of the building precision in the laser engineered net shaping process using advanced networks, Opt. Lasers Eng. 48 (2010) 519–525, http://dx.doi.org/10.1016/j.optlaseng.2010.01.002

[100] D. Srivastava, I.T.H. Chang, M.H. Loretto, The effect of process parameters and heat treatment on the microstructure of direct laser fabricated TiAl alloy samples, Intermetallics 9 (2001) 1003–1013.

[101] X. He, J. Mazumder, Transport phenomena during direct metal deposition, J. Appl. Phys. 101 (2007) 053113, http://dx.doi.org/10.1063/1.2710780

[102] L. Wang, S. Felicelli, Process modeling in laser deposition of multilayer SS410 steel, J. Manuf. Sci. Eng. 129 (2007) 1028–1034, http://dx.doi.org/10.1115/1.2738962

[103] A.J. Pinkerton, L. Li, Modelling the geometry of a moving laser melt pool and deposition track via energy and mass balances, J. Phys. D: Appl. Phys. 37 (2004) 1885–1895, http://dx.doi.org/10.1088/0022-3727/37/14/003

[104] J. Xie, A. Kart, J.A. Rothenflue, W.P. Latham, Temperature-dependent absorptivity and cutting capability of CO_2, Nd:YAG and chemical oxygen-iodine lasers, J. Laser Appl. 9 (1997) 77–85.

[105] Y.S. Lee, M. Nordin, S.S. Babu, F.F. Farson, Influence of fluid convection on weld pool formation in laser cladding, Weld. J. 93 (2014) 292s–300s.

[106] R.R. Unocic, J.N. DuPont, Process efficiency measurements in the laser engineered net shaping process, Metall. Mater. Trans. B 35 (2004) 143–152.

[107] P. Peyre, P. Aubry, R. Fabbro, R. Neveu, A. Longuet, Analytical and numerical modelling of the direct metal deposiion process, J. Phys. D: Appl. Phys. 41 (2008) 025403.

[108] W.M. Steen, Laser material processing – an overview, J. Opt. A Pure Appl. Opt. 5 (2003) 3–7.

[109] H. Qi, J. Mazumder, H. Ki, Numerical simulation of heat transfer and fluid flow in coaxial laser cladding process for direct metal deposition, J. Appl. Phys. 100 (2006) 11, http://dx.doi.org/10.1063/1.2209807

[110] J. Laeng, G. Stewart, F. Liou, Laser metal forming processes for rapid prototyping – a review, Int. J. Prod. Res. 38 (2000) 3973–3996.

[111] S. Sankaranarayanan, A. Kar, Nonlinear effects of laser–plasma interaction on melt-surface temperature, J. Phys. D: Appl. Phys. 32 (1999) 777–784.

[112] F. Vásquez, J.A. Ramos-Grez, M. Walczak, Multiphysics simulation of laser–material interaction during laser powder depositon, Int. J. Adv. Manuf. Technol. 59 (2012) 1037–1045, http://dx.doi.org/10.1007/s00170-011-3571-4

[113] L. Peng, Y. Taiping, L. Sheng, L. Dongsheng, H. Qianwu, X. Weihao, et al., Direct laser fabrication of nickel alloy samples, Int. J. Mach. Tools Manuf. 45 (2005) 1288–1294, http://dx.doi.org/10.1016/j.ijmachtools.2005.01.014

[114] A. Simchi, Direct laser sintering of metal powders: mechanism, kinetics and microstructural features, Mater. Sci. Eng. A 428 (2006) 148–158, http://dx.doi.org/10.1016/j.msea.2006.04.117

[115] S. Wen, Y.C. Shin, Modeling of transport phenomena during the coaxial laser direct deposition process, J. Appl. Phys. 108 (2010) 044908, http://dx.doi.org/10.1063/1.3474655

[116] J.P. Kruth, L. Froyen, J. Van Vaerenbergh, P. Mercelis, M. Rombouts, B. Lauwers, Selective laser melting of iron-based powder, J. Mater. Process. Technol. 149 (2004) 616–622.

[117] Y.-L. Huang, J. Liu, N.-H. Ma, J.-G. Li, Three-dimensional analytical model on laser-powder interaction during laser cladding, J. Laser Appl. 18 (2006) 42–46.

[118] J. Liu, L. Li, Effects of powder concentration distribution on fabrication of thin-wall parts in coaxial laser cladding, Opt. Laser Technol. 37 (2005) 287–292, http://dx.doi.org/10.1016/j.optlastec.2004.04.009

[119] J. Liu, L. Li, Effects of process variables on laser direct formation of thin wall, Opt. Laser Technol. 39 (2007) 231–236, http://dx.doi.org/10.1016/j.optlastec.2005.08.012

[120] U. Articek, M. Milfelner, I. Anzel, Synthesis of functionally graded material H13/Cu by LENS technology, Adv. Prod. Eng. Manag. 8 (2013) 169–176.

[121] W. Liu, J.N. DuPont, Fabrication of functionally graded TiC/Ti composites by laser engineered net shaping, Scr. Mater. 48 (2003) 1337–1342.

[122] F.F. Noecker, J.N. DuPont, Functionally graded copper-steel using laser engineered net shaping process, in: Proc. 13th Solid Free. Fabr. Symp., Austin, USA, 2002, pp. 231–238.

[123] A. Bandyopadhyay, B.V. Krishna, W. Xue, S. Bose, Application of laser engineered net shaping (LENS) to manufacture porous and functionally graded structures for load bearing implants, J. Mater. Sci. Mater. Med. 20 (2009) S29–S34.

[124] K.I. Schwendner, R. Banerjee, P.C. Collins, C.A. Brice, H.L. Fraser, Direct laser deposition of alloys from elemental powder blends, Scr. Mater. 45 (2001) 1123–1129.

[125] Y.Z. Zhang, C. Meacock, R. Vilar, Laser powder micro-deposition of compositional gradient Ti–Cr alloy, Mater. Des. 31 (2010) 3891–3895.

[126] P.C. Collins, R. Banerjee, S. Banerjee, H.L. Fraser, Laser deposition of compositionally graded titanium–vanadium and titanium–molybdenum alloys, Mater. Sci. Eng. A 352 (2003) 118–128, http://dx.doi.org/10.1016/S0921-5093(02)00909-7

[127] W. Liu, J.N. Dupont, In-situ reactive processing of nickel aluminides by laser-engineered net shaping, Metall. Mater. Trans. A 34 (2003) 2633–2641.

[128] D. Wu, X. Liang, Q. Li, L. Jiang, Laser rapid manufacturing of stainless steel 316L/Inconel718 functionally graded materials: microstructure evolution and mechanical properties, Int. J. Opt. (2010), http://dx.doi.org/10.1155/2010/802385, Article ID 802385.

[129] M.L. Griffith, L.D. Harwell, J.T. Romero, E. Schlienger, C.L. Atwood, J.E. Smugeresky, Multi-material processing by LENSTM, in: Proc. 8th Solid Free. Fabr. Symp., Austin, USA, 1997, pp. 387–394.

[130] L. Han, K.M. Phatak, F.W. Liou, Modeling of laser cladding with powder injection, Metall. Mater. Trans. B 35 (2004) 1139–1150.

[131] L. Han, F.W. Liou, S. Musti, Thermal behavior and geometry model of melt pool in laser material process, ASME J. Heat Transfer 127 (2005) 1005, http://dx.doi.org/10.1115/1.2005275

[132] L. Wang, S. Felicelli, Analysis of thermal phenomena in LENS deposition, Mater. Sci. Eng. A 435–436 (2006) 625–631, http://dx.doi.org/10.1016/j.msea.2006.07.087

[133] W. Hofmeister, M. Griffith, M. Ensz, J. Smugeresky, Solidification in direct metal deposition by LENS processing, JOM 53 (2001) 30–34.

[134] M. Alimardani, E. Toyserkani, J.P. Huissoon, Three-dimensional numerical approach for geometrical prediction of multilayer laser solid freeform fabrication process, J. Laser Appl. 19 (2007) 14–25.

[135] J. Kummailil, C. Sammarco, D. Skinner, C. Brown, A.K. Rong, Effect of select LENSTM processing parameters on the deposition of Ti–6Al–4V, J. Manuf. Processes 7 (2005) 42–50.

[136] A. Frenk, M. Vandyoussefi, J.-D. Wagnière, A. Zryd, W. Kurz, Analysis of the laser-cladding process for stellite on steel, Metall. Mater. Trans. B 28 (1997) 501–508.

[137] L. Tang, R.G. Landers, Melt pool temperature control for laser metal deposition processes—Part II: Layer-to-layer temperature control, ASME J. Manuf. Sci. Eng. 132 (2010) 011011, http://dx.doi.org/10.1115/1.4000883

[138] X. He, J.T. Norris, P.W. Fuerschbach, T. DebRoy, Alloying element vaporization and liquid metal expulsion during laser microjoining of stainless steel with short pulse, in: Trends Weld. Res. Proc. 7th Int. Conf. 2005, ASM Int., Pine Mountain, USA, 2006, pp. 109–114.

[139] H. Yin, S. Felicelli, L. Wang, Fluid flow, heat and mass transfer in the molten pool of the LENS process, in: Extr. Process. Div. Congr. 2008 TMS, The Miner. Met. Mater. Soc., New Orleans, 2008, pp. 261–270.

[140] A. Kumar, S. Roy, Effect of three-dimensional melt pool convection on process characteristics during laser cladding, Comput. Mater. Sci. 46 (2009) 495–506, http://dx.doi.org/10.1016/j.commatsci.2009.04.002

[141] Y.P. Lei, H. Murakawa, Y.W. Shi, X.Y. Li, Numerical analysis of the competitive influence of marangoni flow and evaporation on heat surface temperature and molten pool shape in laser surface remelting, Comput. Mater. Sci. 21 (2001) 276–290.

[142] M.E. Thompson, J. Szekely, The transient behavior of weldpools with a deformed free surface, Int. J. Heat Mass Transfer 32 (1989) 1007–1019.

[143] M. Picasso, A.F.A. Hoadley, Finite element simulation of laser surface treatments including convection in the melt pool, Int. J. Numer. Methods Heat Fluid Flow 4 (1994) 61–83.

[144] G.N. Ellison, Maximum thermal spreading resistance for rectangular sources and plates with nonunity aspect ratios, IEEE Trans. Comp. Pack. Technol. 26 (2003) 439–454.

[145] S.M. Thompson, H.B. Ma, Thermal spreading analysis of rectangular heat spreader, ASME J. Heat Transfer 136 (2014) 064503, http://dx.doi.org/10.1115/1.4026558

[146] R.T.C. Choo, J. Szekely, The possible role of turbulence in GTA weld pool behavior, Weld. J. Res. Suppl. 73 (1994) 25s–31s.

[147] N. Chakraborty, S. Chakraborty, Distinct influences of turbulence in momentum, heat and mass transfers during melt pool convection in a typical laser surface alloying process, Eur. Phys. J. Appl. Phys. 36 (2006) 71–89.

[148] D. Chatterjee, S. Chakraborty, Entropy generation analysis of turbulent transport in laser surface alloying process, Mater. Sci. Technol. 22 (2006) 627–633, http://dx.doi.org/10.1179/174328406X83978

[149] N. Kumar, S. Dash, A.K. Tyagi, B. Raj, Melt pool vorticity in deep penetration laser material, Sadhana 36 (2011) 251–265.

[150] L. Wang, S. Felicelli, Y. Gooroochurn, P.T. Wang, M.F. Horstemeyer, Optimization of the LENS process for steady molten pool size, Mater. Sci. Eng. A 474 (2008) 148–156, http://dx.doi.org/10.1016/j.msea.2007.04.119

[151] A. Fathi, A. Mozaffari, Vector optimization of laser solid freeform fabrication system using a hierarchical mutaable smart bee-fuzzy inference system and hybrid NSGA-II/self-organizing map, J. Intell. Manuf. 25 (2014) 775–795.

[152] M. Labudovic, D. Hu, R. Kovacevic, A three dimensional model for direct laser metal powder deposition and rapid prototyping, J. Mater. Sci. 38 (2003) 35–49.

[153] V. Neela, A. De, Three-dimensional heat transfer analysis of LENS process using finite element method, Int. J. Adv. Manuf. Technol. 45 (2009) 935–943, http://dx.doi.org/10.1007/s00170-009-2024-9

[154] S. Wen, Y.C. Shin, Comprehensive predictive modeling and parametric analysis of multitrack direct laser deposition processes, J. Laser Appl. 23 (2011) 022003, http://dx.doi.org/10.2351/1.3567962

[155] H. Yin, S.D. Felicelli, Multi-scale solidification model for laser engineered net shaping (LENS) process, in: Extr. Process. Div. Congr. 2010 TMS, The Miner. Met. Mater. Soc., Seattle, 2010, pp. 571–579.

[156] S.A. David, J.M. Vitek, Correlation between solidification parameters and weld microstructures, Int. Mater. Rev. 34 (1989) 213–245.

[157] W. Kurz, C. Bezençon, M. Gäuman, Columnar to equiazed transition in solidification processing, Sci. Technol. Adv. Mater. 2 (2001) 185–191.

[158] H. Yin, S.D. Felicelli, Dendrite growth simulation during solidification in the LENS process, Acta Mater. 58 (2010) 1455–1465, http://dx.doi.org/10.1016/j.actamat.2009.10.053

[159] M. Rappaz, Modelling of microstructure formation in solidification processes, Int. Mater. Rev. 34 (1989) 93–123.

[160] S.M. Kelly, S.L. Kampe, Microstructural evolution in laser-deposited multilayer Ti–6Al–4V builds: Part II. Thermal modeling, Metall. Mater. Trans. A 35 (2004) 1869–1879.

[161] D.P. Kennedy, Spreading resistance in cylindrical semiconductor devices, J. Appl. Phys. 31 (1960) 1490–1497.

[162] D. Rosenthal, The theory of moving sources of heat and its application to metal treatments, Trans. Am. Soc. Mech. Eng. 68 (1946) 849–866.

[163] N. Christensen, V. Davies, K. Gjermundsen, Distribution of temperature in arc welding, Br. Weld. J. 12 (1965) 54–75.

[164] N.N. Rykalin, A.V. Nikolaev, Welding arc heat flow, Weld. World 9 (1971) 112–133.

[165] D.T. Swift-Hook, A.E.F. Gick, Penetration welding with lasers, Weld. J. 52 (1973) 492s–499s.

[166] J.G. Andrews, D.R. Atthey, Hydrodynamic limit to penetration of a material by a high-power beam, J. Phys. D: Appl. Phys. 9 (1976) 2181–2194.

[167] J. Mazumder, W.M. Steen, Heat transfer model for CW laser material processing, J. Appl. Phys. 51 (1980) 941, http://dx.doi.org/10.1063/1.327672

[168] T.W. Eagar, N.-S. Tsai, Temperature fields produced by traveling distributed heat sources, Weld. J. (1983) 346–355.

[169] N.T. Nguyen, A. Ohta, K. Matsuoka, N. Suzuki, Y. Maeda, Analytical solutions for transient temperature of semi-infinite body subjected to 3-D moving heat sources, Weld. J. 78 (1999) 265S–274S.

[170] J. Goldak, A. Chakravarti, M. Bibby, A new finite element model for welding heat source, Metall. Trans. B 15B (1984) 299–305.

[171] A. Vasinonta, J. Beuth, M. Griffith, Process maps for laser deposition of thin-walled structures, in: Proc. 10th Solid Free. Fabr. Symp., Austin, USA, 1999, pp. 383–392.

[172] W.M. Steen, J. Dowden, M. Davis, P. Kapadia, A point and line source model of laser keyhold welding, J. Phys. D: Appl. Phys. 21 (1988) 1255–1260.

[173] P.G. Klemens, Heat balane and flow conditions for electron beam and laser welding, J. Appl. Phys. 47 (1976) 2165–2174.

[174] G.W. Krutz, L.J. Segerlind, Finite element analysis of welded structures, Weld. J. Res. Suppl. 57 (1978) 211s–216s.

[175] L. Costa, R. Vilar, T. Réti, Simulating the effects of substrate pre-heating on the final structure of steel parts built by laser powder deposition, in: Proc. 15th Solid Free. Fabr. Symp., Austin, USA, 2004, pp. 643–654.

[176] R. Long, W. Liu, F. Xing, H. Wang, Numerical simulation of thermal behavior during laser metal deposition shaping, Trans. Nonferrous Met. Soc. China 18 (2008) 691–699.

[177] A. Crespo, R. Vilar, Finite element analysis of the rapid manufacturing of Ti–6Al–4V parts by laser powder deposition, Scr. Mater. 63 (2010) 140–143, http://dx.doi.org/10.1016/j.scriptamat.2010.03.036

[178] R. Paul, S. Anand, F. Gerner, Effect of thermal deformation on part errors in metal powder based additive manufacturing processes, J. Manuf. Sci. Eng. 136 (2014) 031009, http://dx.doi.org/10.1115/1.4026524

[179] C.P. Patel, R.I. Patel, 3D heat transfer analysis and numerical modeling of LENS process for thin wall by using Stainless Steel 304, Int. J. Mod. Eng. Res. 2 (2012) 1596–1601.

[180] T. Purtonen, A. Kalliosaari, A. Salminen, Monitoring and adaptive control of laser processes, Phys. Proc. 56 (2014) 1218–1231, http://dx.doi.org/10.1016/j.phpro.2014.08.038

[181] A. Gülhan, Application of Pyrometry and IR-Thermography to High Surface Temperature Measurements, RTO AVT Course Meas. Tech. High Enthalpy Plasma Flows, Rhode-St-Genèse, Belgium: RTO-EN-8, 1999, 9B1–9B24.

[182] R.P. Madding, Emissivity measurement and temperature correction accuracy considerations, in: SPIE Conf. Thermosense XXI, Orlando, USA, 1999, pp. 393–401.

[183] G. Bi, C. Sun, A. Gasser, Study on influential factors for process monitoring and control in laser aided additive manufacturing, J. Mater. Process. Technol. 213 (2013) 463–468.

[184] A. Yadollahi, D. Seely, B. Patton, N. Shamsaei, S.M. Thompson, Mechanical and Microstructural Properties of LENS-Produced AISI 316L Stainless Steel, in: 56th AIAA/ASCE/AHS/ASC Structures, Structural Dynamics, and Materials Conference, Kissimmee, FL, 2015, http://dx.doi.org/10.2514/6.2015-1355

[185] A.O. Kerbrat, P. Mognol, J.-Y. Hascoët, A new DFM approach to combine machining and additive manufacturing, Comput. Ind. 62 (2011) 684–692.

[186] J. Francis, T.E. Sparks, J. Ruan, F. Liou, Multi-axis tool path generation for surface finish machining of a rapid manufacturing process, Int. J. Rapid Manuf. 4 (2014) 66–80, http://dx.doi.org/10.1504/IJRAPIDM.2014.062040

[187] B. Rosa, P. Mognol, J. Hascoët, Laser polishing of additive laser manufacturing surfaces, J. Laser Appl. 27 (2015) S29102, http://dx.doi.org/10.2351/1.4906385

[188] K.P. Karunakaran, S. Suryakumar, V. Pushpa, S. Akula, Low cost integration of additive and subtractive processes for hybrid layered manufacturing, Robot. Comput. Integr. Manuf. 26 (2010) 490–499, http://dx.doi.org/10.1016/j.rcim.2010.03.008

[189] ASTM-International, ASTM Standard ASTM F2971-13: Standard Practice for Reporting Data for Test Specimens Prepared by Additive Manufacturing, 2013, West Conshohocken.

[190] L.P. Schanwald, Two Powder Stream Diagnostics for Laser Deposition Processes, Proceedings of the 14th International Congress on Applications of Lasers & Electro-Optics (ICALEO), San Diego, USA, 1995, pp. 660–669.

Glossary

AM: additive manufacturing
CA: cellular automation
CAD: computer aided design/drawing
CCD: semiconductor charge-coupled devices
CCT: continuous cooling transformation
CFD: computational fluid dynamics
CMOS: complementary metal–oxide–semiconductor
CNC: computer numerical control
DAS: dendrite arm spacing
DED: directed energy deposition
DLD: direct laser deposition
DLMPD: direct laser metal powder deposition
EB: electron beam
EDM: electrical discharge machining
EM: electromagnetic
FEM: finite element method
FGM: functionally graded material
HAZ: heat affected zone
LADRM: laser-aided direct rapid manufacturing
LBAM: laser-based additive manufacturing
LENS: laser engineering net shaping
PBL-L: powder bed fusion-laser
PDS: powder delivery system
PREP: plasma rotating electrode process
SEM: scanning electron microscope
SFF: solid freeform fabrication
SLM: selective laser melting
STL: standard tessellation language
TPS: triangulation position sensor